0427S

EUROPEAN ORGANIZATION FOR NUCLEAR RESEARCH

CERN - SPS DIVISION

SPS/ABT/Tech. Note 86-4

THE CONSTRUCTION OF ELECTROSTATIC SEPTA WITH INVAR ANODES AND ULTRA-THIN WIRES

R. L. Keizer, R. Oberli

Prévessin, June 1986

C O N T E N T S

APPENDICES

SYMBOLS, DIMENSIONS AND VALUES USED IN THIS REPORT

a	(m)	=	spacing of the septum wires [1.5×10^{-3}]
A	($V\ m^{-1}$)	=	constant
A_{loc}	(m^2)	=	cross section of the region where the electron beam has molten the metal [2.5×10^{-5}]
B	(V)	=	constant
c	($m\ s^{-1}$)	=	velocity of light [3×10^{8}]
C_a	(m)	=	internal depth of the anode [0.179]
C_{ox}	($J\ kg^{-1}\ °C^{-1}$)	=	specific heat of the anodised layer [880]
C_{wo}	($J\ m^{-3} °C^{-1}$)	=	volumetric heat of tungsten [2.7×10^{6}]
d	(µm)	=	diameter of the septum wires [100 and 65 for respectively the stainless and INVAR anodes]
d_a	(m)	=	external width of the anode [0.230]
d_n	(m)	=	horizontal distance between the rear of the anode and the neutral line [0.080]
d_1	(µm)	=	deformation of the upper septum nose
d_2	(µm)	=	deformation of the lower septum nose

D_{wo} (m^2 s^{-1}) = diffusivity of tungsten [$6.5\ 10^{-5}$]

e (C) = e.s charge of the electron [$1.6\ 10^{-19}$]

E_a (MPa) = modulus of elasticity of the INVAR anode [2.1×10^5]

E_g ($V\ m^{-1}$) = average gradient in the anode - cathode region [10^7]

E_m ($V\ m^{-1}$) = maximum average gradient avoiding field-emission

E_{ox} (MPa) = coefficient of elasticity of the anodised layer [5×10^4]

E_r ($V\ m^{-1}$) = e.s. field measured on the surface of the septum wire

E_y ($V\ m^{-1}$) = transversal component of the e.s. field in the median plane

E_{yo} ($V\ m^{-1}$) = average e.s. field just outside the septum plane

f(o), f(z) ($P\ m^{-2}$) = proton distribution functions

f_d = field dilution factor caused by the septum wire configuration [0.98]

f_f = coefficient of static friction between septum wire and anode

f_p (µm) = deflection of the p-beam by one e.s. septum

f_{pi} (μm) = deflection of the p-beam at the end of the i^{th} e.s. septum

f_s (μm) = sagitta of the curved septum plane

G_y ($V\ m^{-2}$) = average transversal field gradient between the septum wires

h (m) = inter-electrode gap [0.020]

h_b (m) = beam height [0.003]

h_i (m) = clearance between ion-trap and anode [0.002 for the stainless steel anode and 0.004 for the INVAR anode]

I (A) = p-beam equivalent electrical current

I_{cl} (A) = clearing current in the ion-traps

J_a (m^4) = 2nd moment of inertia of the anode for bending in the horizontal plane [3.7×10^{-5}]

k_2 ($m^{-3}\ K\ Torr^{-1}$) = constant [9.65×10^{-24}]

k_I (A m) = constant [7.64×10^{-12}]

k_{ox} ($W\ m^{-1}\ °C^{-1}$) = thermal conductivity of the anodised layer [37]

k_{wo} ($W\ m^{-1}\ °C^{-1}$) = thermal conductivity of tungsten [175]

l_c	(m)	=	length of a curved segment of the anode [0.050]
l_e	(m)	=	electrical length of an e.s septum [3.130]
l_{ei}	(m)	=	electrical length of the ion-traps [3.3]
l_i	(m)	=	distance between two insulators of the ion-traps in longitudinal direction [0.300]
l_r	(m)	=	length of a straight segment of the anode [0.100]
l_s	(m)	=	mechanical length of the anode or the septum [3.120]
l_z	(m)	=	free length of a septum wire
n		=	number of septum wires [2.000]
n_+	(m^{-3})	=	equivalent density of the nitrogen gas for ionisation
N_o		=	number of protons falling on the first septum wire
N_n		=	number of protons after nuclear scattering by n wires
N_p	(ppp)	=	number of protons per pulse in the circulating beam
N_{pin}	(ppp)	=	maximum number of protons per pulse which may be extracted with an INVAR anode

N_{pst}	(ppp)	=	maximum number of protons per pulse which may be extracted with a stainless steel anode
p	(GeV c^{-1})	=	proton momentum [450]
P_+	(Torr)	=	N_2 equivalent ionisation pressure [10^{-7}]
P_{pd}		=	proton loss percentage due to electrostatic dilution of the beam
P_{pn}		=	proton loss percentage due to nuclear scattering by the septum wires
R	(m)	=	radius of the cylindrical surface of the nose of the anode
R_a	(m)	=	average radius of the curved anode [7.2 x 10^3]
R_c	(m)	=	radius of the curved section of the anode [2.4 10^3]
R_s	(°C m $s^{-½}$)	=	coefficient of thermal endurance
R_{SPS}	(m)	=	radius of the SPS [1100]
s	(μm)	=	vertical sag of the anode measured in the median plane
t_{in}	(μm)	=	effective septum thickness using an INVAR anode

t_{st} (μm) = effective septum thickness using a stainless steel anode

T (°C) = temperature of the anode and the ion-trap

T_A (k) = absolute temperature of the residual gas [300]

T_c (°C) = temperature of the cathode during the bake-out [80]

T_f (N) = frictional force between the septum wire and the anode

T_N (N) = normal component of the tensile force caused by the wire spring

T_o (N) = tensile force in the septum wire caused by the wire spring

V (V) = negative potential of the cathode [2×10^5]

V_1 (V) = potential caused by an infinite array of septum wires

V_2 (V) = potential which creates a uniform transversal e.s. field

W_d (μm) = width of the electrostatically diluted p-beam at the end of the first septum

x (m) = longitudinal coordinate in the direction of the beam

x_d (m) = length of the drift space between e.s septa (0.790)

y (m) = transversal coordinate starting in the septum plane

y_{max} (μm) = deflection of the septum wires by the electrostatic force, in the median plane

z (m) = vertical coordinate starting in the median plane

ZS_i = the i^{th} septum, $1 \leq i \leq 5$

α (rad) = rotation of a segment of the anode

α_a ($°C^{-1}$) = linear coefficient of thermal expansion of stainless steel [16×10^{-6}]

α_{al} ($°C^{-1}$) = linear coefficient of thermal expansion of PERALUMAN [23×10^{6}]

α_i ($°C^{-1}$) = linear coefficient of thermal expansion of the ion-trap [16×10^{-6}]

α_{ox} ($°C^{-1}$) = linear coefficient of thermal expansion of the anodised layer [5×10^{-6}]

β = relative proton velocity at 450 GeV/c [1]

γ (rad) = constant

ΔE	($J\ kg^{-1}\ m^{-2}$)	=	minimum ionisation energy of 450 GeV/c protons. [2.30×10^{-14}]
ΔQ	($J\ m^{-3}$)	=	specific energy loss
ΔQ_w	(J)	=	energy loss per septum wire
ΔT	(°C)	=	adiabatic temperature rise of the centre of the wire
ΔT_{sa}	(°C)	=	temperature difference between ion-trap and anode causing a short-circuit
ΔT_y	(°C)	=	difference in temperature across the anode in transversal direction
ε_o	($A\ s\ V^{-1}m^{-1}$)	=	permeability of vacuum [$8.859\ 10^{-12}$]
ε_{ox}		=	strain in the anodised layer on the cathode
θ	(rad)	=	arbitrary angle
θ_f	(rad)	=	angle of deflection of a septum wire [70° or 0.61 rad]
λ	($A\ s\ m^{-1}$)	=	constant
λ_s	(m)	=	scattering length of protons in tungsten [0.1]
ρ_{ox}	($kg\ m^{-3}$)	=	density of the anodised layer [3900]

ρ_{wo}	(kg m^{-3})	=	density of tungsten [19200]
σ_s		=	standard deviation of the vertical proton beam profile
σ_N	(m^2)	=	ionization cross section of N_2 [1.2×10^{-22}]
σ_{loc}	(MPa)	=	local tensile stress in the electron-beam welded region of the anode profile
σ_{ox}	(MPa)	=	tensile stress in the anodised layer caused by differential thermal expansion
σ_{tox}	(MPa)	=	ultimate tensile strength of the anodised alumina [200]
ν	(mrad)	=	angle of electrostatic deflection of the protons caused by one septum [6.96×10^{-2}]

1. INTRODUCTION

The extracted beam intensity has been increasing steadily since the start of fixed target physics, first in LSS6 from 1976 onwards and later in LSS2 from 1978 onwards.

The first signs of excessive spark rate have been recorded end 1979 [1] when for fast-resonant extraction of 9×10^{12} ppp the ion-traps became inoperative after only 15 min.

During other performance tests [2] similar behaviour was observed after 2 hours of stable operation of 1.8×10^{13} ppp fast-resonant extracted. Later reports [3,4] indicate that 8×10^{12} ppp constituted the upper limit for reliable operation of fast resonant extraction.

For slow-extraction the spark rate became very high at 1.2×10^{13} ppp. This was revealed by a spark rate analysis [5] covering several months of operation. The construction of dedicated electronics made it possible to do parasitic machine development studies and to discern between normal and abnormal operating conditions, thereby allowing considerable data reduction. It was then possible to observe during normal operation linear relationships between extracted intensity, beam loss and spark rate.

Thereafter it was discovered, using the same dedicated electronics in conjunction with semi-automatic data transfer to the IBM computer, allowing to speed up the analysis, that the septa deformed thermally in a measurable and repeatable way [6] when the extracted intensity reached 10^{13} ppp.

In the meantime the erratic behaviour of the ion-traps was traced down to buckling and short-circuiting caused by differential expansion due to radiation heating.

A prototype sliding ion-trap was therefore constructed which was designed to prevent buckling under thermal stress. Tests [7] then showed

that up to 1.6 x 10^{13} ppp, the highest intensity the SPS was capable of extracting at that time in LSS2, the voltage holding capacity of the sliding version remained unimpaired. The ion-traps positioned lower down the beam line in ZS3 and ZS4 all short-circuited in the end.

Finally, it was demonstrated[8] that, for small temperature differences across the anode, thermal deformation easily doubles the effective septum thickness. The proposition then was made to use INVAR as construction material instead of stainless steel and to employ thinner septum wires.

A third limit was reached end 1983 when due to teething troubles with the novel shared extraction, two septa were lost because of feedthrough failure[9]. This problem was finally cured by modifying the oil circulation system[10].

In order to make a comparison possible between the existing and the INVAR septa, spark analysis was carried out on a daily routine basis. Beam losses were recorded for each pulse[11]. Therefore, when the first INVAR septum started operating, measurements immediately showed an enormous improvement. The beam losses were reduced by a factor of 2 to 3 (12).

At present, both extraction channels LSS2 and LSS6, contain INVAR septa as the first two elements. As a result the extracted intensity can now exceed 2 x 10^{13} ppp per channel.

2. THE EXISTING SEPTA

2.1. The stainless steel anode

The construction of the 3120 mm long anode is shown in Fig. 1.

The body consists of a stainless steel U-profile which acts as a frame on which the septum wires are stretched and aligned. Inside are mounted the 1 mm thick electrodes which form the upper and lower ion-traps.

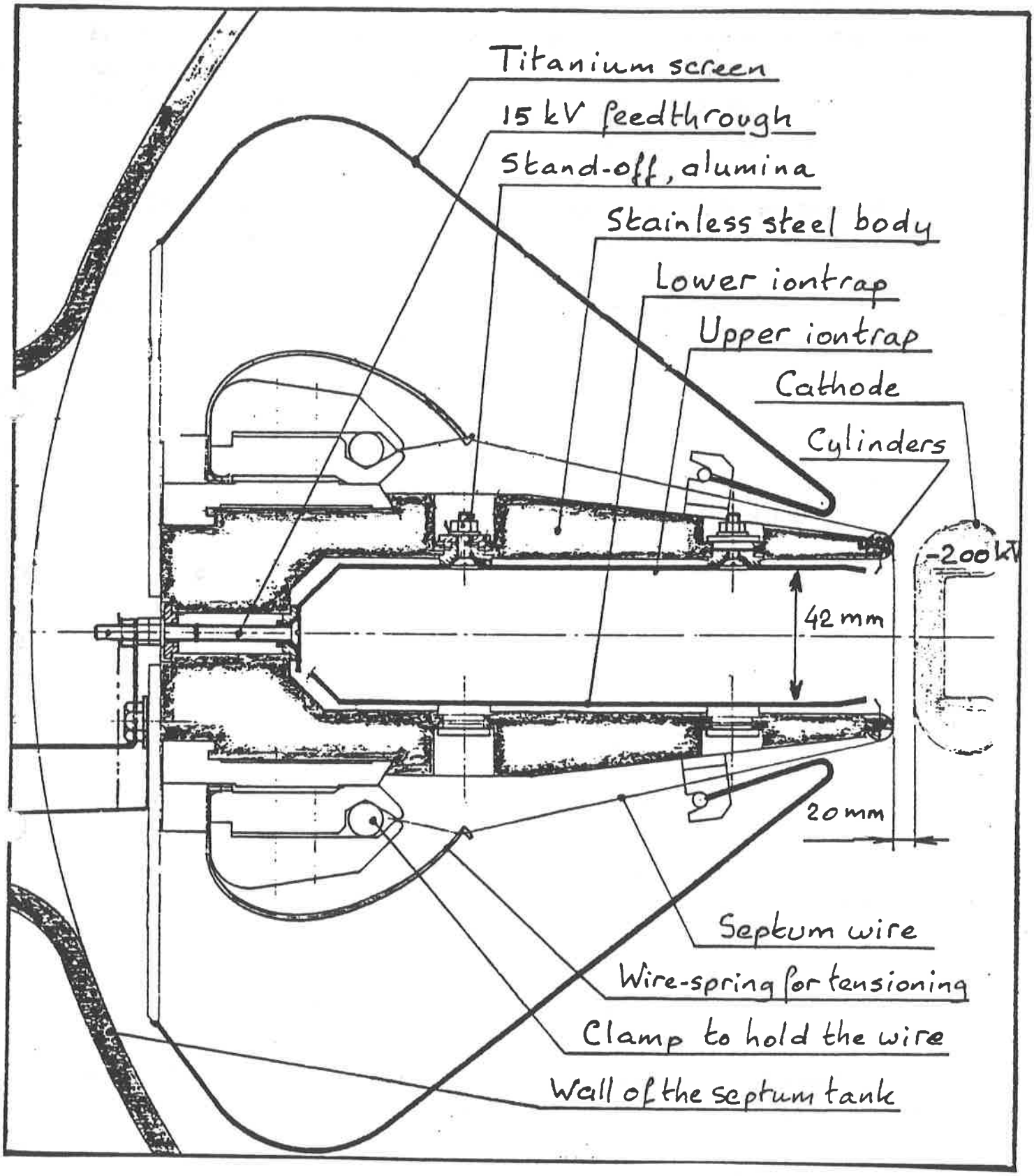

Fig. 1 **Construction of the stainless steel anode**

The anode is electrically isolated from earth to allow monitoring of the anode current and the spark signals. Two remotely controlled electric motors, one at the upstream and one at the downstream end, can displace the anode horizontally, over a distance of 2 mm, for alignment with the other septa which form the extraction channel.

The problem with the anode body is that the secondary particles, scattered by the septum wires, heat the body of the anode. The secondaries move forward in a sharp cone. The stainless steel tips near the septum wires therefore heat up more than regions of the anode body further away. The septum therefore deforms which doubles or triples the 150 μm effective septum thickness and increases proportionally the beam losses.

The transversal thermal gradient causes the anode body to bend in the horizontal plane with a radius of curvature directed to the centre of the SPS. The sagitta f_s of the septum is then given by[8] :

$$f_s = \frac{10^6 \ \alpha_a \ l_s^2 \ \Delta T_y}{8 \ d_a} \qquad (1)$$

For an anode with a coefficient of thermal expansion $\alpha_a = 16 \times 10^{-6}$ $°C^{-1}$, a length $l_s = 3.120$ m and width $d_a = 0.230$ m, a doubling of the effective septum thickness, with $f_s = 150$ μm, is expected to occur with a temperature difference across the anode of $\Delta T_y = 1.8$ °C. The sensitivity for thermal deformation then may be expressed by the constant :

$$\frac{f_s}{\Delta T_y} = 85 \ \mu m \ °C^{-1} \qquad (2)$$

Furthermore the anode is made of one piece which renders manufacturing expensive and limits the shape of the profile.

2.2 The ion-traps

The ions, created by collision of the circulating beam with the residual gas, are captured by two electrodes, the upper and the lower ion-traps which are shown in Fig. 1. Both traps are charged negatively with respect to the anode and therefore attract positive ions, thus preventing them from impinging on the cathode causing secondary emission and sparks. The high voltage is applied via 15 kV feedthroughs located in the body of the anode.

The electrodes are electrically insulated, using alumina stand-offs, which rigidly link the ion-traps to the anode.

The weakness of this construction is that there is a strong tendency for the 1 mm thick electrodes, spaced at 2 mm from the anode, to buckle when heated by the secondaries scattered from the septum. The ion-traps are in general nearer to the beam and are therefore warmer than the surrounding electrode which, in addition, acts as a thermal screen.

For a sinusoidal deformation as shown in Fig 2, the temperature at which a short-circuit occurs is given by :

$$\Delta T_{sa} = \frac{1}{\alpha_i} \left[\frac{\pi \ h_i}{2 \ l_i} \right]^2 \qquad (3)$$

where l_i is the distance between the two stand-offs or fixed points, h_i the clearance between ion-trap and anode. For the existing ion-traps $l_i = 0.3$ m, $h_i = 0.002$ m, $\alpha_i = 16 \times 10^{-6}$ °C^{-1}. Therefore a small temperature difference of only 7 °C already causes a short-circuit.

Visual inspection of the ion-traps indicates the presence of regions half-way in between the stand-offs, where strong spark erosion occurred.

2.3. Septum wires and effective septum thickness

The septum wires are stretched over accurately machined cylinders, shown in Fig. 1, which are aligned with a precision of 20 μm.

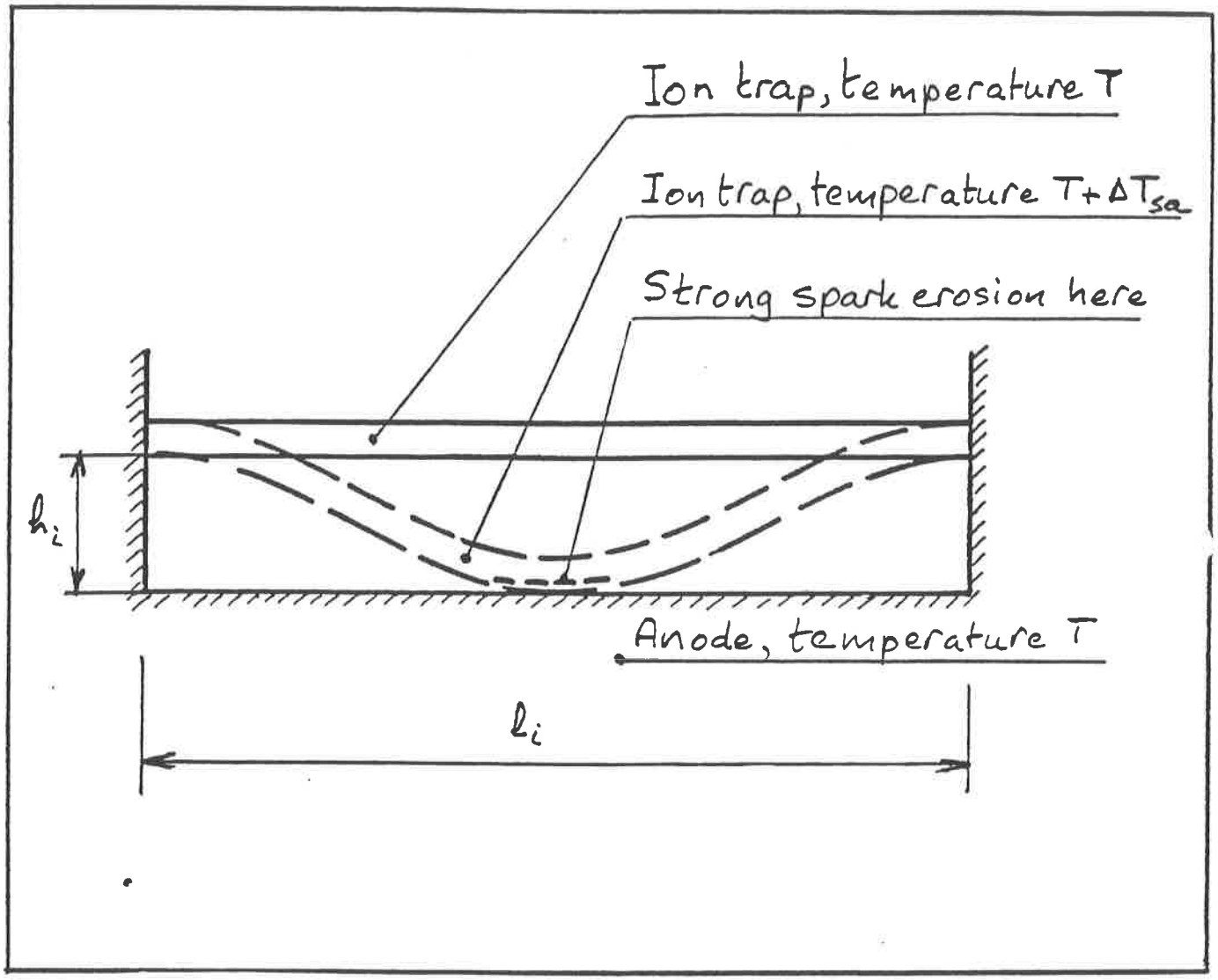

Fig. 2 Buckling of the ion-traps due to differential heating

The wires are made of 100 µm thick WoRe material[17]. Wire-springs, 1 mm in diameter, ensure a tensile force of approximately 5 N which is roughly 20% of their breaking strength. Wire-springs have been selected because of the large displacement. In the event of one of the wires being damaged by the circulating beam, the wire-springs will pull the two ends from the dangerous inter-electrode region.

The high frictional force between the wire and the cylinder is a disadvantage because septum wires heat to some 200-400 °C during extraction and the loss in tensile force is not fully compensated.

A problem with the cylinders is that for accurate alignment, the diameter and the straightness thereof must be very precise and that the anode tip against which they repose must be very straight. This method of construction is very expensive.

The choice of the wire diameter depends on the straightness which can be finally obtained. If the straightness is 20 μm then it is natural to use wires of equivalent thickness. However, there is a lower limit determined by the onset of secondary emission. This happens in the case of polarity reversal which is required for anti-proton injection.

For positively charged wires, field emission starts at a gradient of some 10^7 V m^{-1}. The gradient E_r on the wire is then given[13] as

$$E_r = \frac{10^6\ a}{\pi\ \ d}\ E_m < 10^7\ V\ m^{-1} \qquad (4)$$

where d is the diameter of the wires which are spaced at distance a. The maximum average gradient between anode and cathode is E_m. For d = 100μm and a = $1{\cdot}5 \times 10^{-3}$ m follows that the maximum average gradient is $E_m = 2 \times 10^6$ V m^{-1}. In practice, values around 3×10^6 V m^{-1} are still safe[18].

It should be noted that the wires are not perfectly smooth everywhere and generally have an elliptical cross section.

The effective septum thickness, using 2000 wires of 100 μm diameter which are stretched over accurately ground stainless steel cylinders which, in turn, are aligned by a 3.120 m long stainless steel anode, is 150 μm. This is only the case at room temperature. Using thinner wires under these circumstances would not appreciably reduce the effective septum thickness.

2.4 The cathode

The 3 m long cathode is made of PERALUMAN PRE 30 (97% Al, 3% Mg) which has been oxidized to a thickness of 8 - 10 μm by anodisation in a chromic acid bath and then sealed in boiling water. Electric fields of 1.8×10^7 V m^{-1} have been obtained but operation is usually at 1.0×10^7 V m^{-1} in order to keep the spark rate down to an acceptable level in the highly radioactive environment.

The position is shown schematically in Fig. 1. Two electrically driven insulating shafts remotely position the cathode. The maximum horizontal displacement is 0.050 m.

The cathode is quite porous and therefore acts as a getter pump under high vacuum conditions once perfectly outgassed. This implies that after a long shutdown the spark rate is high initially. The tank without cathode, is outbakable at 300°C. However, once the cathode is mounted, the temperatures may never exceed 80°C because of the degradation of the oxide layer.

The thermal degradation is two-fold :

- The coefficient of thermal expansion, α_{ox}, of the anodised layer consisting of Al_2O_3 is 5×10^{-6} $°C^{-1}$ and that of PERALUMAN, α_{al}, is 23×10^{6} $°C^{-1}$. At a temperature T_c of 80°C the strain in the oxide ε_{ox} will then be, assuming there is no strain at 20°C

$$\varepsilon_{ox} = (\alpha_{al} - \alpha_{ox})\,(T_c - 20) = 1 \cdot 1 \times 10^{-3} \qquad (5)$$

The tensile stress in the anodised layer, σ_{ox}, with a coefficient of elasticity of $E_{ox} = 5 \times 10^4$ MPa then becomes

$$\sigma_{ox} = \varepsilon_{ox} E_{ox} = 54 \text{ MPa} \qquad (6)$$

This is roughly one-third of the ultimate tensile strength of Al_2O_3. It has been reported that for chromic acid anodisation cracks become quite visible at strains of $15\ 10^{-3}$.

-At 350 °C Al_2O_3 looses its crystal water and becomes amorphous.

The advantage of an anodised layer of Al_2O_3, because of its porous structure, is that the thermal shock resistance measured by the coefficient of thermal endurance, R_s, is rather high.

For Al_2O_3 is found that :

$$R_s = \frac{\sigma_{tox}}{E_{ox}\ \alpha_{ox}} \left[\frac{k_{ox}}{\rho_{ox}\ C_{ox}} \right]^{1/2} \approx 0.33 \text{ °C m s}^{-1/2} \qquad (7)$$

The following values have been taken. The ultimate tensile strength $\sigma_{tox} = 200$ MPa, the thermal conductivity $k_{ox} = 37$ W $m^{-1}°C^{-1}$, the specific weight is $\rho_{ox} = 3\ 900$ kg m^{-3} and the specific heat $C_{ox} = 880$ J $kg^{-1}°C^{-1}$. This means that sparks will less likely damage the oxide layer than is the case with titanite ceramic with $R_s \approx 0.10$. The energy of the ions should be such that they are fully absorbed in the anodised layer and do not penetrate into the aluminium cathode itself.

3. CONSTRUCTION OF THE IMPROVED SEPTA

3.1 The INVAR anode

With INVAR the septum doubling transversal temperature difference will be $\Delta T_y = 32$ °C instead of the 1.8°C reported in section 2.1.

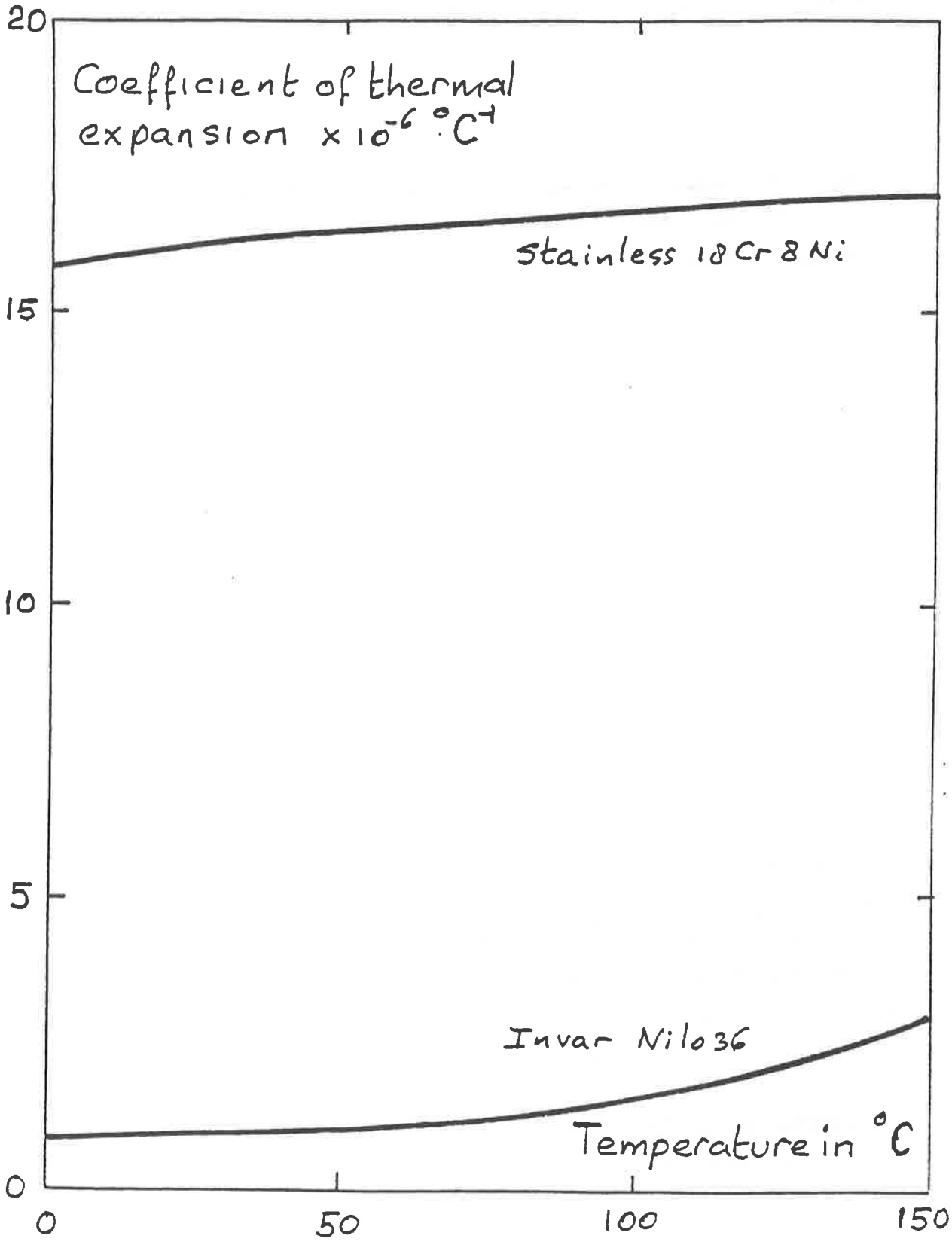

Fig. 3 The thermal expansion of several alloys

The thermal expansion of several alloys is shown in Fig. 3. Compared with stainless steel the expansion of INVAR is a factor of 18 less. A temperature rise of 1.8 °C will therefore increase the septum thickness of 100 μm by 6% only.

A second consequence is that because the septum deforms less, much more proton intensity, N_{pin}, may be extracted than was the case before N_{pst}, to obtain the same temperature rise.

$$N_{pin} = \frac{t_{st}}{t_{in}} N_{pst} \approx 3 N_{pst} \qquad (8)$$

where t_{in} is the INVAR septum thickness, 106 μm and t_{st} the previous septum thickness, 300 μm at $\Delta T_y = 1.8°C$.

The anode is assembled from 3 pieces, as shown in Fig. 4 to make the construction more economic and to allow machining of the V-groove.

Because the beam shrinks during acceleration, the septum height at the level of the noses may be reduced from 46 to 38 mm. The noses rigidify the anodes and prevent secondaries from entering directly the space between the ion-traps and the anode and striking the insulators. The reduction of the length of the septum wires also improves the alignment because the wires are full of internal stress and are not straight at all when left free.

The machining of 3m long INVAR bars with a straightness of 20 μm is not easy and many intermediate heat treatments are necessary (see Appendix 1).

The anode is first assembled by screws and dowel-pins. Hereafter, two discontinuous argon-arc weldings are made along the rearside. These weldings will reduce the deformation of the anode body caused by the tension in the septum wires. The discontinuous weldings will also deform the anode in the horizontal plane.

Consider a profile of length l_s and average radius R_a, as shown in Fig. 5, consisting of n identical elements. Each element is formed by

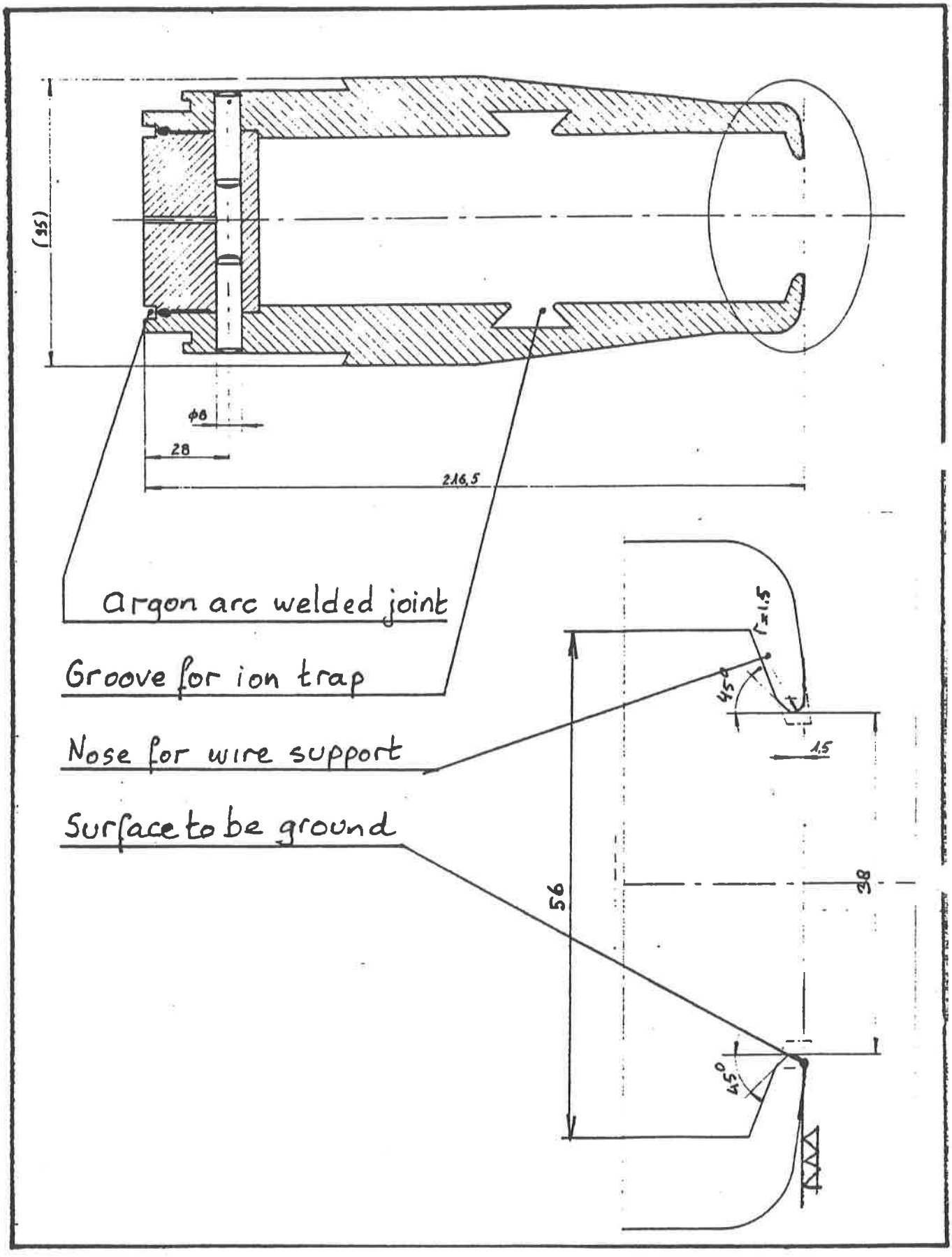

Fig. 4 Construction of the INVAR anode

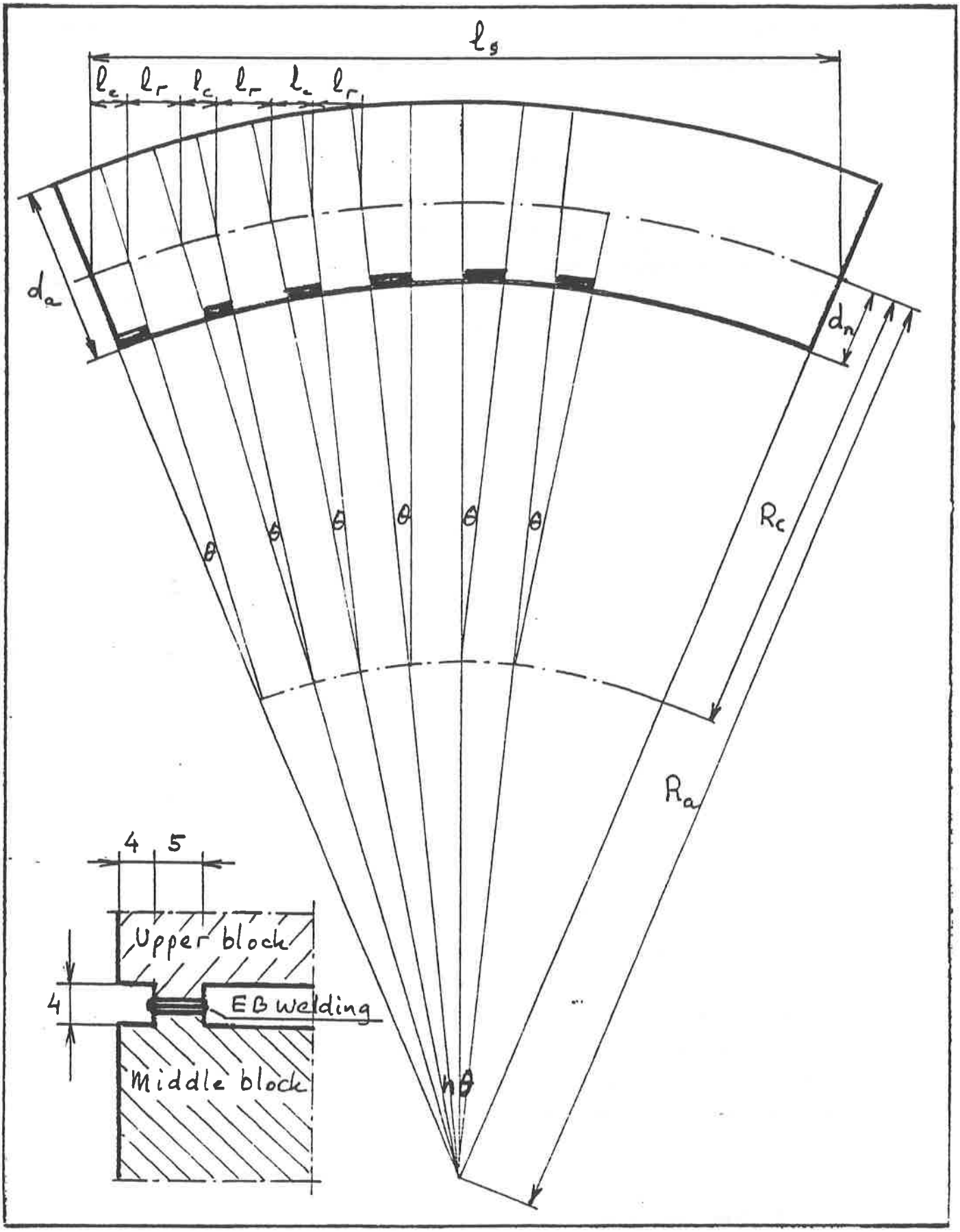

Fig. 5 Curvature of the anode caused by E.B. welding

a curved part with radius R_c, length l_c and a straight part of length l_r. Simple geometrical considerations show that

$$R_c = \frac{l_c}{l_c + l_r} R_a \tag{9}$$

Assume now that the curvature R_c is caused by a contraction of a certain volume of molten material along the length l_c at distance d_n from the neutral line. The local tensile stress is σ_{loc} and the cross section of each electron beam welding is A_{loc}. The following relation is then valid:

$$\frac{1}{R_c} = \frac{2\ \sigma_{loc}\ A_{loc}\ d_n}{E_a\ J_a} \tag{10}$$

With $R_a = 7.2 \times 10^3$ m, $l_c = 0.050$ m, $l_r = 0.100$ m, $E_a = 2.1 \times 10^5$ MPa, $J_a = 3.7 \times 10^{-5} m^4$, dn = 0.080 m, $A_{loc} = 2.5 \cdot 10^{-5} m^2$, follows that $\sigma_{loc} = 800$ MPa which is quite realistic.

The sagitta f_s is then given by:

$$f_s = \frac{10^6\ l_s^2}{8\ R_a} \tag{11}$$

with the existing parameters $f_s \approx 170$ µm.

The final machining operation therefore consists of grinding approximately 0.2 mm from the septum noses, as shown in Fig. 4, lower figure. The septum should thereby be supported at both ends by blocks which simulate the suspension in the tanks. The sag introduced by its own weight causes an additional curvature in the horizontal plane. This point is elaborated in Appendix 2. One could go even one step further by introducing special clamps which simulate the force exercised by the septum wires.

3.2 Sliding Ion-traps

The construction is shown in Fig. 6, upper drawing. The upper and lower ion-traps are suspended and centred by spherical insulators made of

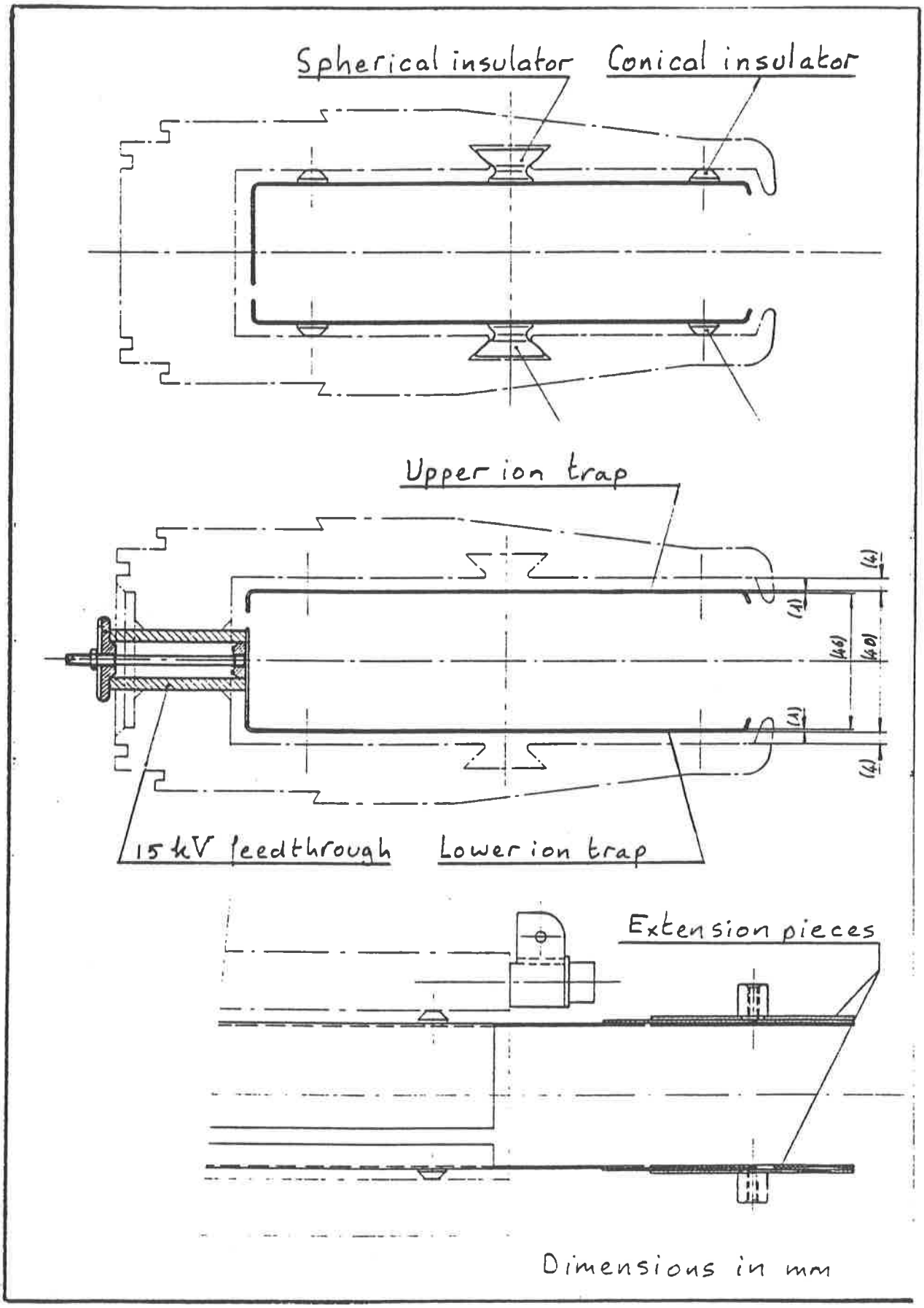

Fig. 6 Construction of the sliding ion-traps

alumina. The small conical insulators on either side serve to maintain parallelism with the anode body.

The middle figure shows the 15 kV feedthrough for the lower ion-trap which is made of one alumina cylinder.

The lower figure shows the extension pieces on the upstream or downstream side of the septum designed to create an electrostatic field beyond the physical length of the septum which increases the ion-trapping efficiency.

Thermal expansion of the ion-traps now is translated into a horizontal displacement without internal stresses, the 15 kV feedthroughs being the fixed points. Buckling is no longer possible, provided the sliding friction remains below 120 N.

The electrodes are L-shaped in cross section. This not only makes them more rigid but also shields the 15 kV insulators from secondaries scattered from the septum wires and cathode.

3.3 The ultra-thin septum wires

In order to exploit the new possibilities of an anode which is much less sensitive to differential heating, the wire diameter has been reduced from 100 to 65 μm.

Field emission from positively charged wires, using equation (4), would then start at $E_m = 1.4 \times 10^6$ V m^{-1} theoretically. However, measurements indicate that in practice fields as high as 3×10^6 V m^{-1} are tolerable. Thinner wires therefore do not seem to lead to stronger field emission when antiprotons are injected into the SPS.

The wires, produced by repeated annealing and drawing have a diameter of 80 μm initially. They are then polished electrolytically using NaHOH as electrolyte. The diameter thereby reduces to roughly 65 μm. Finally follows mechanical testing by stretching to 50% of the ultimate breaking strength, which is 4 10^3 MPa, to eliminate any weak spots.

The frictional force between the wire and the anode has been a point of concern because the straightness of each wire depends on it.

The wire springs, shown in Fig. 1, stretch the 100 μm diameter wires with a force T_o of 5N and the 65 μm diameter wires with roughly 1 N.

Using a static friction coefficient f_f, the frictional force T_f, as shown in Fig. 7, is then a function of the angle of deflection θ_f of the wire and may be calculated as follows.

$$T_f = T_o \, [e^{f_f \theta_f} - 1] \tag{12}$$

Therefore, if the deformation of the surfaces in contact on the septum nose is negligible, the friction is independent of the radius R of the cylindrical surface shown in Fig. 7. In practice, however, the polishing of the septum wire is not perfect and variations of the frictional force of the order of 100% have been measured.

The average values of the frictional force T_f, using 65 μm diameter wire and two different noses, are shown in Fig. 8 as a function of the tensile force.

For $T_o < 0.5$ N the coefficient of static friction is 0.7 which is already quite high. For higher values of T_o the friction increases quite non linearly.

The two radii yield different values of the frictional force, the smallest radius giving rise to a force which is some 30% higher.

This shows that there is considerable deformation of the contact surface and equation (12) cannot be applied for forces exceeding 0.5 N.

The wires are subjected to electrostatic forces and are deflected towards the cathode as shown in Fig. 9. The displacement y_{max} in the median plane may then be expressed by

$$y_{max} = \frac{\varepsilon_o \, f_d \, a \, E_g^2 \, l_z^2}{16 \, (T_o - T_f)} \tag{13}$$

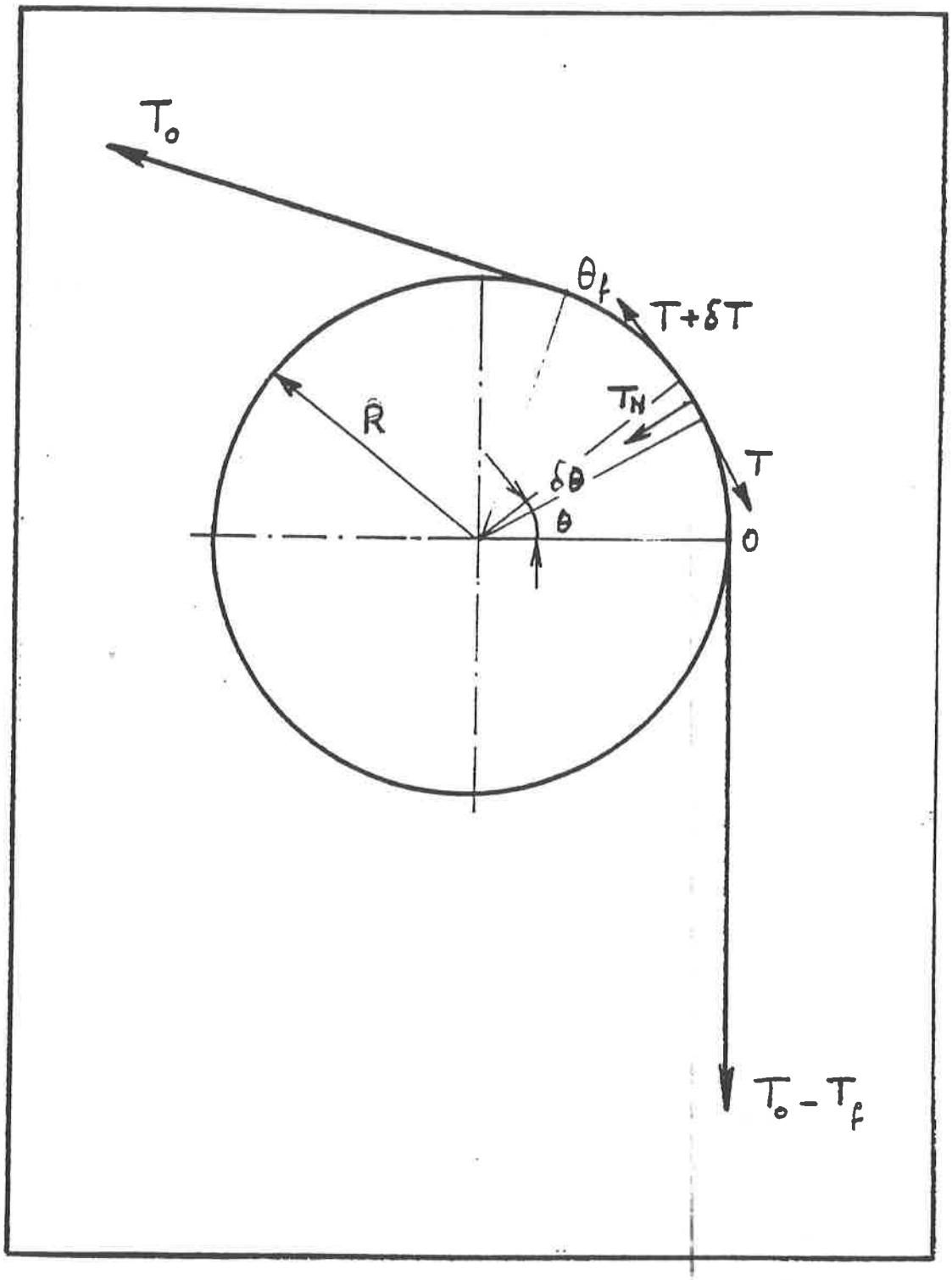

Fig. 7 Analysis of the forces in the wire

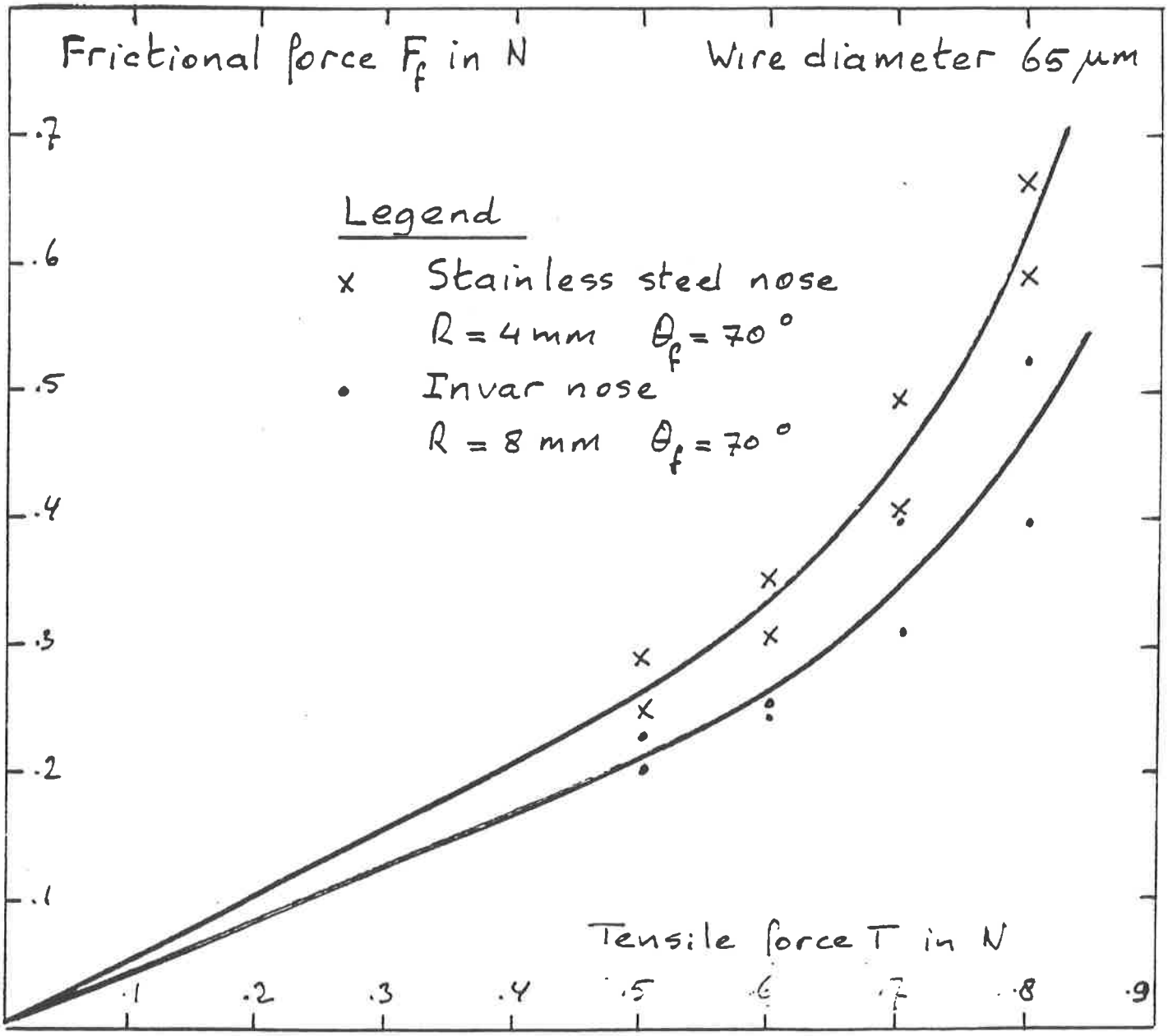

Fig. 8 Friction with stainless steel and INVAR noses

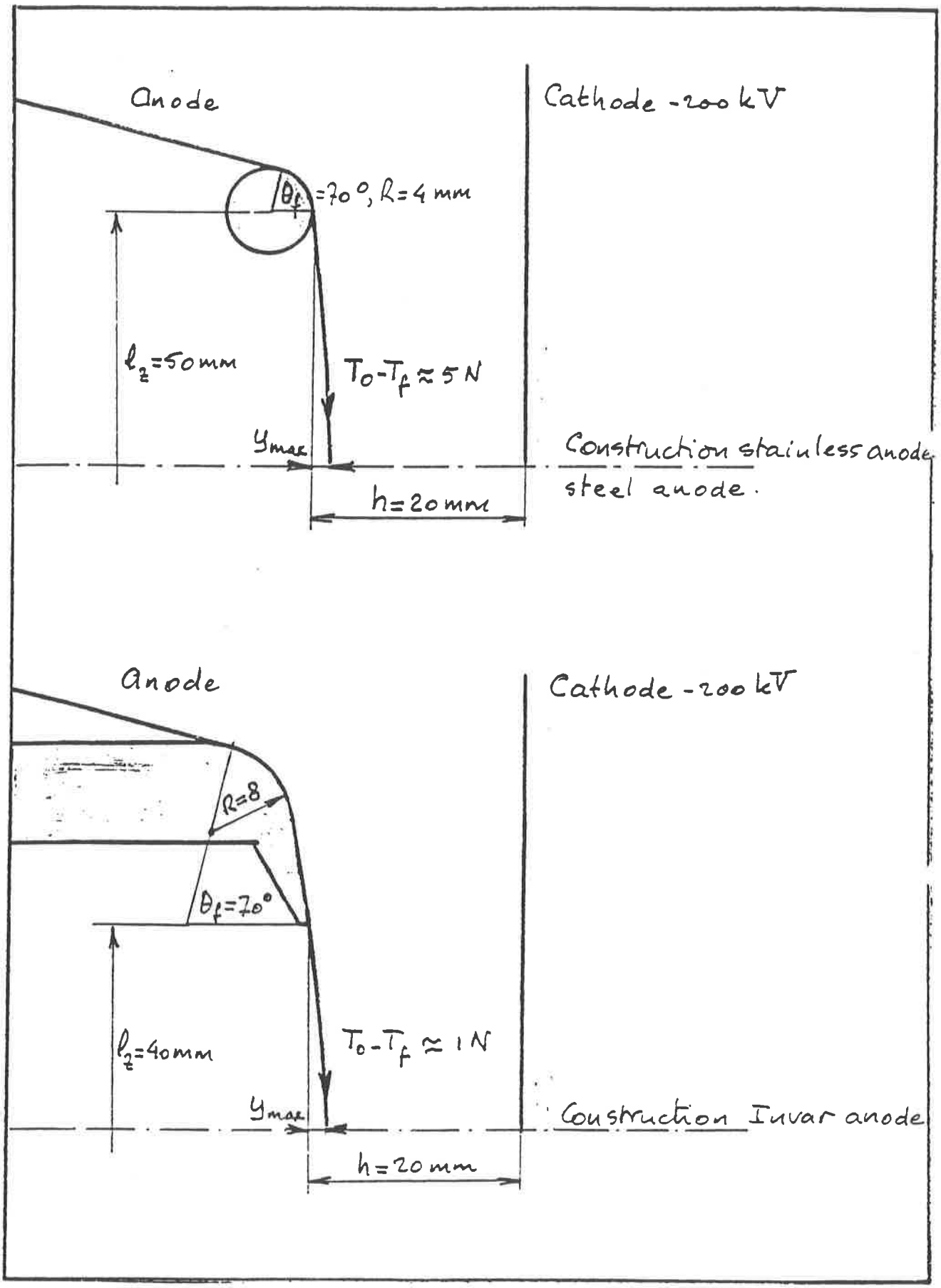

Fig. 9 Suspension of the septum wires

where l_z is the length of the septum wire and f_d is the field dilution factor defined by equation (17), Fig. 12.

Substituting the values shown in Fig. 9 and with $f_d = 0.98$ a deflection of 130 μm is found. Therefore irregular friction and reduced attraction in the end-field regions, may cause a scattering in the position of the septum wires of some 100 μm, which is considerable.

4. PHYSICAL PARAMETERS

4.1 Required straightness of a septum

4.1.1 Electrostatic deflection of the beam

The angle of deflection ν for protons by one septum is given by

$$\nu(\text{mrad}) = 10^3 \text{ atan } [10^{-9} \frac{E_g \, l_e}{\beta \, p}] \qquad (14)$$

and the deviation f_p at the end of the first septum then becomes:

$$f_p \ (\mu\text{m}) = 500 \, l_e \, \nu \qquad (15)$$

where E_g is the electrostatic field V m^{-1}

l_e is the electrical length [m]

p is the proton momentum Gev/c

β is the relative proton velocity.

For one septum length and 450 GeV/c protons, see Fig. 10, the deflection $\nu = 6.96 \times 10^{-2}$ mrad and the deviation if $f_p = 109$ μm. Hence the deviation is of the same order as the thickness of the septum wires.

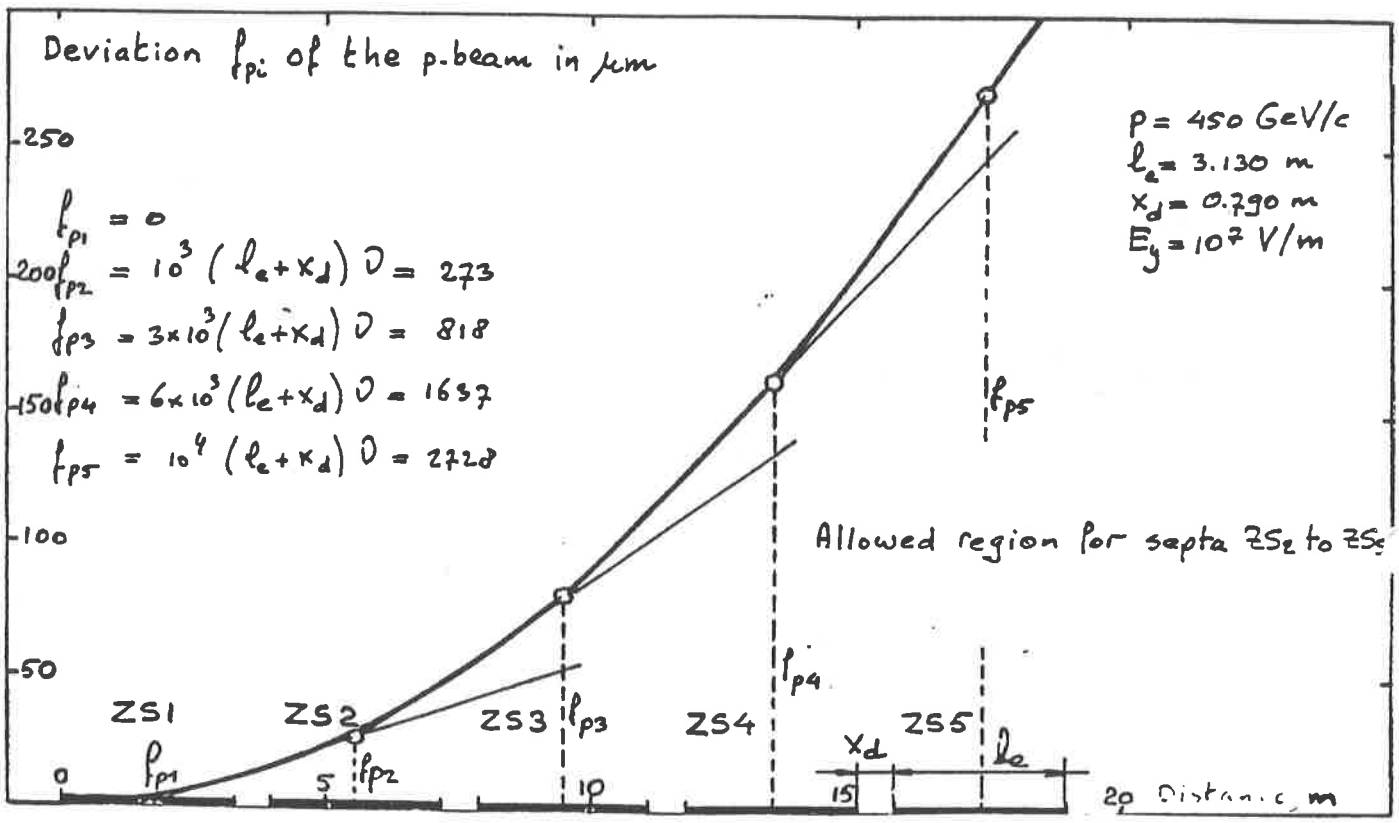

Fig. 10 **Electrostatic deflection of the proton beam**

4.1.2 Extraction with deformed septa

This section treats the question of whether the second septa should also be made of INVAR.

The situation where all the septa following the first one are deformed, is shown in Fig. 11. For the second septum made of stainless steel a deformation of 100% is quite normal, much larger thermal deformations have already been observed. If the second septum is made of INVAR the thermal deformation will remain below 10%.

It is seen that if the first septum is reduced to 100 μm, additional losses by a conventional second septum become unavoidable. A similar study of deformed septa in phase space has been made leading to the same conclusion.

It is therefore necessary to replace the first two extraction elements by INVAR septa.

4.1.3 Beam losses in a wire septum

Exact calculations of beam losses caused by wire septa are extremely complicated because of the absence of any axial symmetry and the complexity of the interactions involved. The only approach therefore which has been attempted is in the form of inspired guesswork.

Several processes contribute to the beam losses:

- Multi-Coulomb Scattering: It can be shown using a number of simplifying assumptions that in the horizontal plane at the end of the first septum, with 2000 wires of 100 μm diameter, all perfectly aligned, only 6% of the particles are scattered out of the septum plane.

- Dilution of the beam by the electric field in between the septum wires. The electrostatic problem has been treated by Durand[13]. The geometry and formulae are shown in Fig. 12. Appendix 3 treats the problem in more detail.

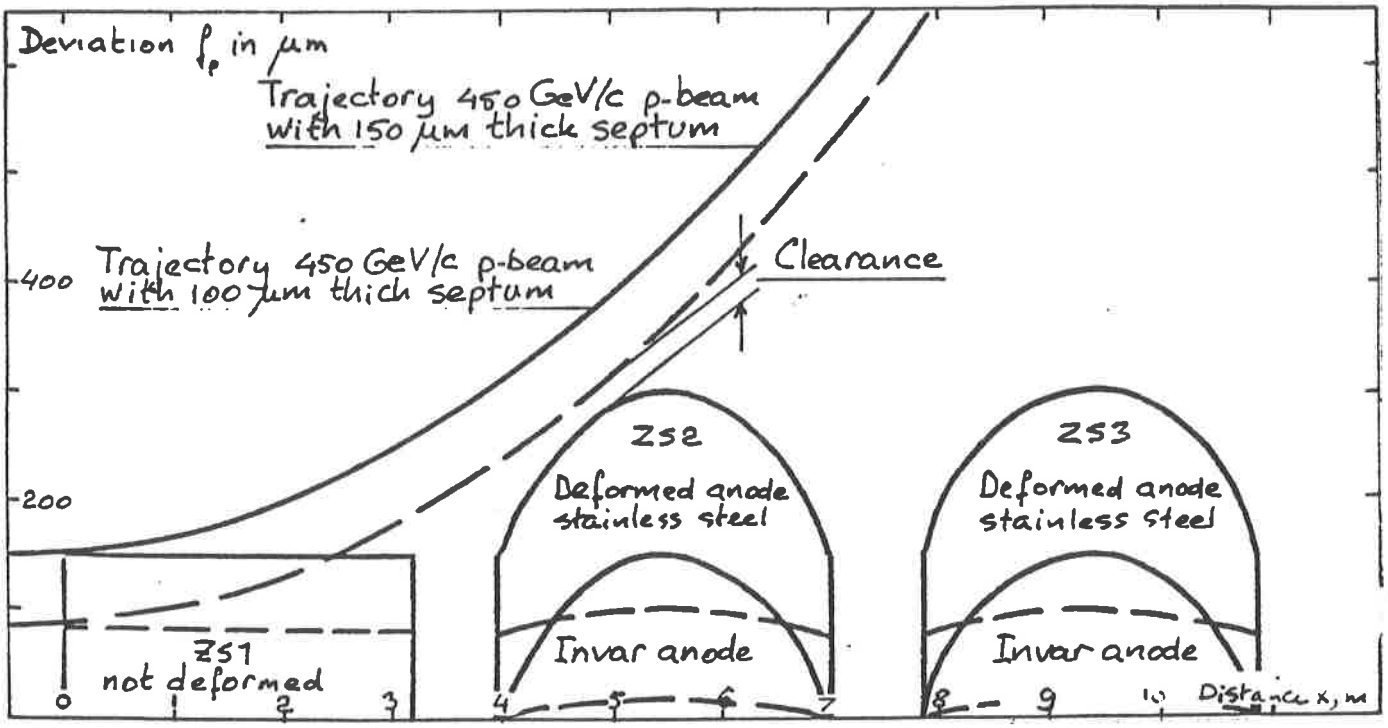

Fig. 11 **Extraction with deformed septa ZS2 to ZS5**

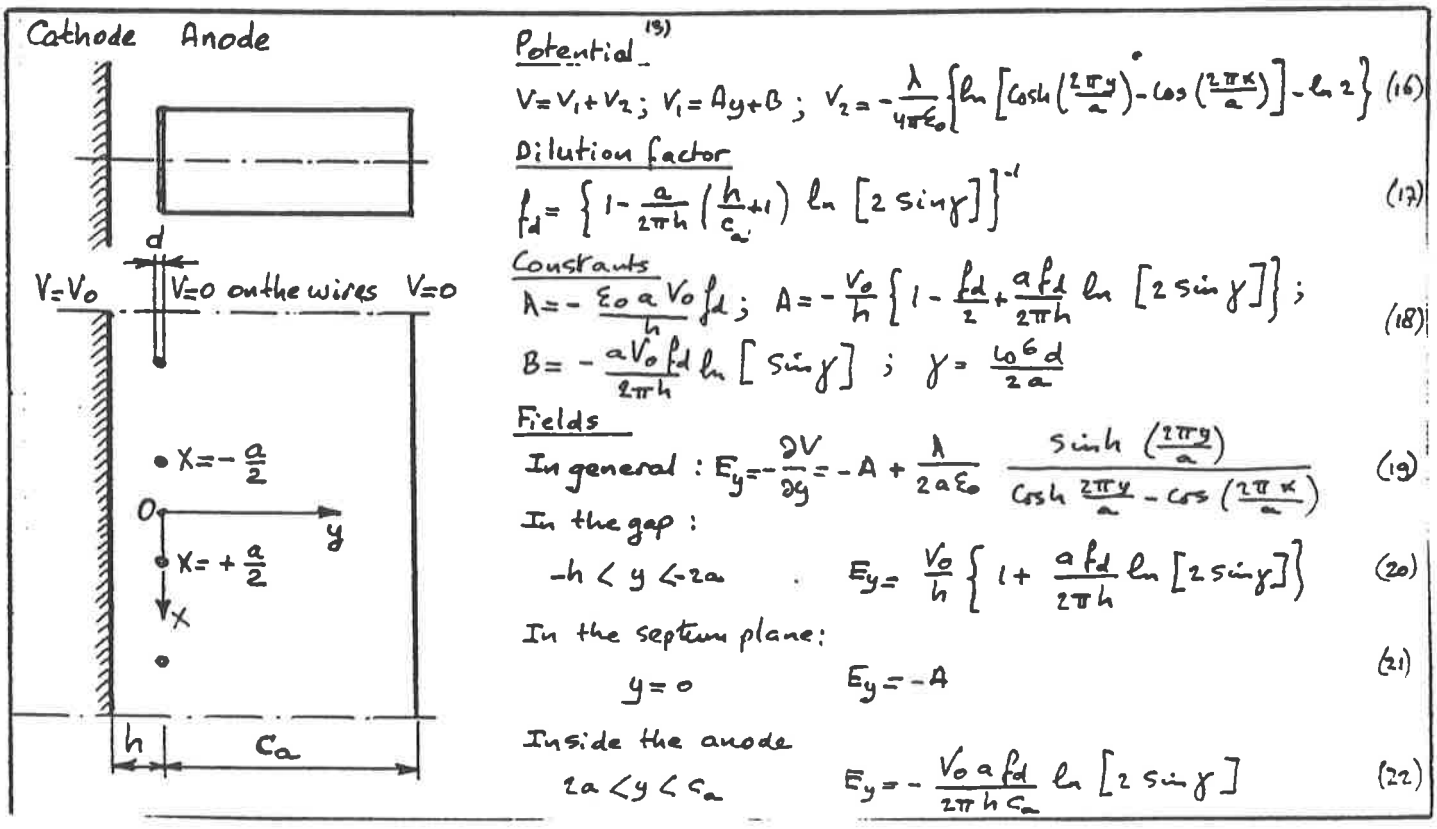

Potential [13]

$$V = V_1 + V_2 ; \quad V_1 = Ay + B ; \quad V_2 = -\frac{\lambda}{4\pi\varepsilon_0}\left\{\ln\left[\cosh\left(\frac{2\pi y}{a}\right) - \cos\left(\frac{2\pi x}{a}\right)\right] - \ln 2\right\} \quad (16)$$

Dilution factor

$$f_d = \left\{1 - \frac{a}{2\pi h}\left(\frac{h}{c_a}+1\right)\ln\left[2\sin\gamma\right]\right\}^{-1} \quad (17)$$

Constants

$$A = -\frac{\varepsilon_0 a V_0 f_d}{h} ; \quad A = -\frac{V_0}{h}\left\{1 - \frac{f_d}{2} + \frac{a f_d}{2\pi h}\ln\left[2\sin\gamma\right]\right\} ;$$

$$B = -\frac{a V_0 f_d}{2\pi h}\ln\left[\sin\gamma\right] ; \quad \gamma = \frac{\pi d}{2a} \quad (18)$$

Fields

In general : $$E_y = -\frac{\partial V}{\partial y} = -A + \frac{\lambda}{2a\varepsilon_0}\,\frac{\sinh\left(\frac{2\pi y}{a}\right)}{\cosh\frac{2\pi y}{a} - \cos\left(\frac{2\pi x}{a}\right)} \quad (19)$$

In the gap :

$$-h < y < -2a \qquad E_y = \frac{V_0}{h}\left\{1 + \frac{a f_d}{2\pi h}\ln\left[2\sin\gamma\right]\right\} \quad (20)$$

In the septum plane:

$$y = 0 \qquad E_y = -A \quad (21)$$

Inside the anode

$$2a < y < c_a \qquad E_y = -\frac{V_0 a f_d}{2\pi h c_a}\ln\left[2\sin\gamma\right] \quad (22)$$

Fig. 12 **Septum geometry and field solutions according to Ref. 13**

The data given are: a wire diameter of d = 100 μm, a wire spacing a = 0.0015 m, an inter-electrode gap h = 0.020 m, an anode depth of C_a = 0.179 m and a potential V = 2 X 10^5 V, from which follows that the field dilution factor f_d = 0.98 and that the transversal component of the field in the septum plane at the centre in between the wires E_y = 4.9 X 10^6 V m^{-1}. The field inside the anode is only 2 X 10^4 V m^{-1} and therefore may be neglected.

With the equations shown in Appendix 3, we calculate that the average field in the septum plane is as high as 6.6 X 10^6 V m^{-1} and that as a result 42% of the particles are extracted due to beam dilution by the electrostatic quadrupole field between the wires.

- Nuclear Scattering: It can be shown, see Appendix 4, that through the mechanism of nuclear scattering 79% of the protons are removed from the septum plane at the end of the first septum.

Combining the three effects one may conclude that at the end of the first septum only 12% of the protons remain. Therefore the straightness and the alignment of the first septum is of crucial importance, the alignment of the second septum is much less critical and the remaining septa are all in the shadow of the first two.

4.2 Electrostatic calculations

4.2.1 The basic principle of ion-trapping

The electrical circuit of the ion-traps is shown in Fig. 13. The upper and lower electrodes each have their own power supply and are charged negatively to 4 or 5 kV with respect to the anode.

The beam will create positive ions and electrons by interaction with the rest gas. The positive ions, if not trapped, will be attracted by the cathode through the wire septum and could thereby trigger sparks.

The ion-traps may be operated in two different ways:

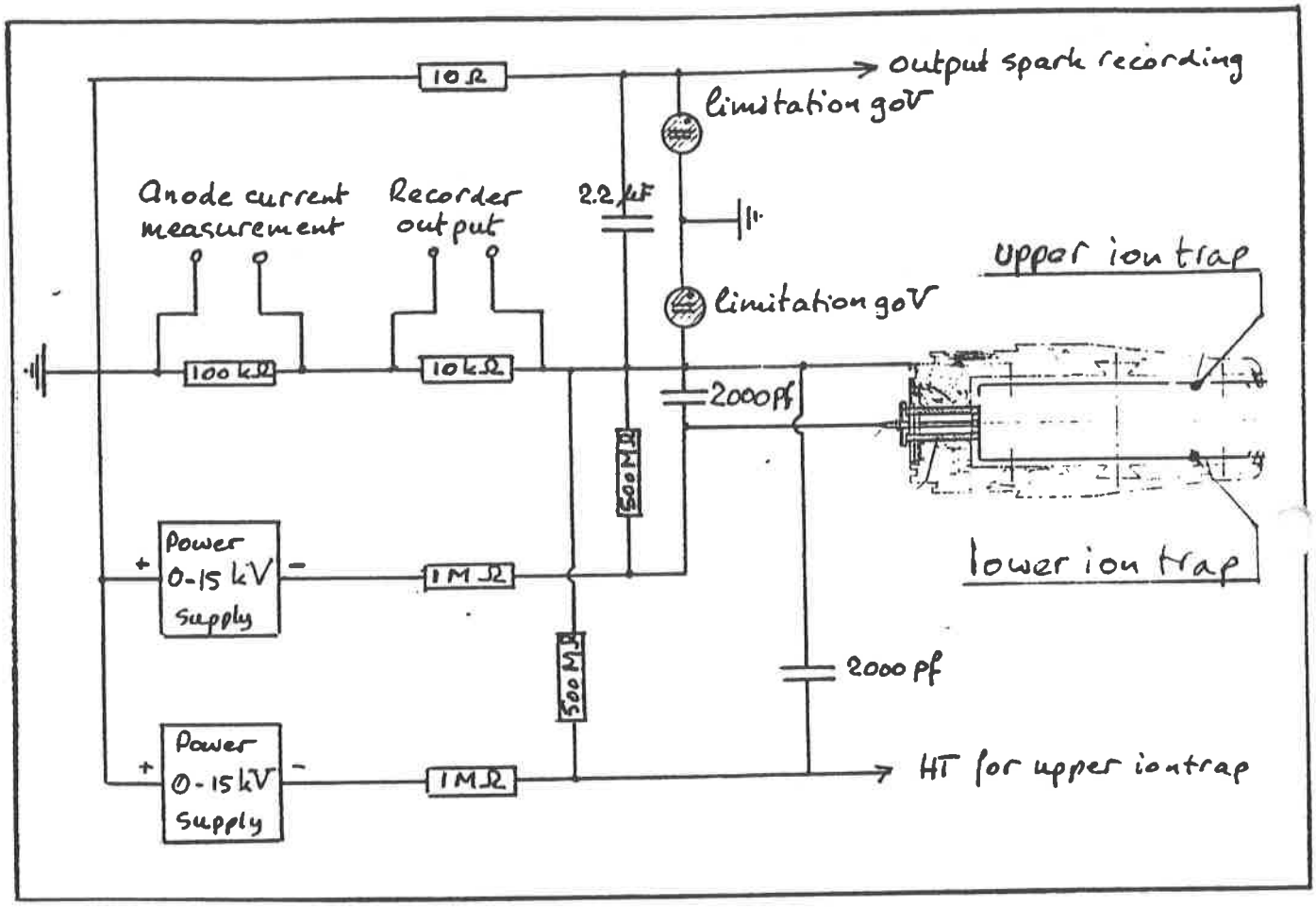

Fig. 13 The HV - Circuit of the ion-traps

- The upper and lower electrodes are charged to the same negative potential. The field plot, see Fig. 14, upper figure, shows that in this case the ions are collected by both the upper and the lower electrodes. The electrons will all move towards the median plane and then will drift to the centre of the septum wires.

- The upper and lower electrodes are charged to slightly different potentials. This is shown in fig. 14 on the lower figure. A vertical electrostatic field is thus created which causes the ions to drift towards the more negative upper electrode. The electrons are now captured partly by the lower electrode and by the septum wires. The number of electrons falling on the septum wires is therefore diminished which results in a considerable reduction of the spark rate[14].

4.2.2 The expected clearing currents

A circulating beam[15] of intensity N_p protons per pulse, represents an average current I of

$$I = \frac{k_I \beta N_p}{R_{SPS}} \qquad (23)$$

where $k_I = e\ c\ (2\pi)^{-1} = 7.64 \times 10^{-12}$ A m, the radius R_{SPS} of the SPS is 1100 m and $\beta = 1$ at 450 GeV/c with $N_p = 10^{13}$ ppp the average current is 0.070 A.

The ionisation of the residual gas produces ions and electrons which give rise to a clearing current I_{cl}. Sputtering of metal atoms by ions has been neglected in this calculation.

$$I_{cl} = \sigma_N\ n_+\ l_{ei}\ I \qquad (24)$$

where
- σ_N is the ionisation noise section of N_2 [m^2]
- n_+ is the molecular density [m^{-3}]
- l_{ei} is the length over which electrons are cleared [m]

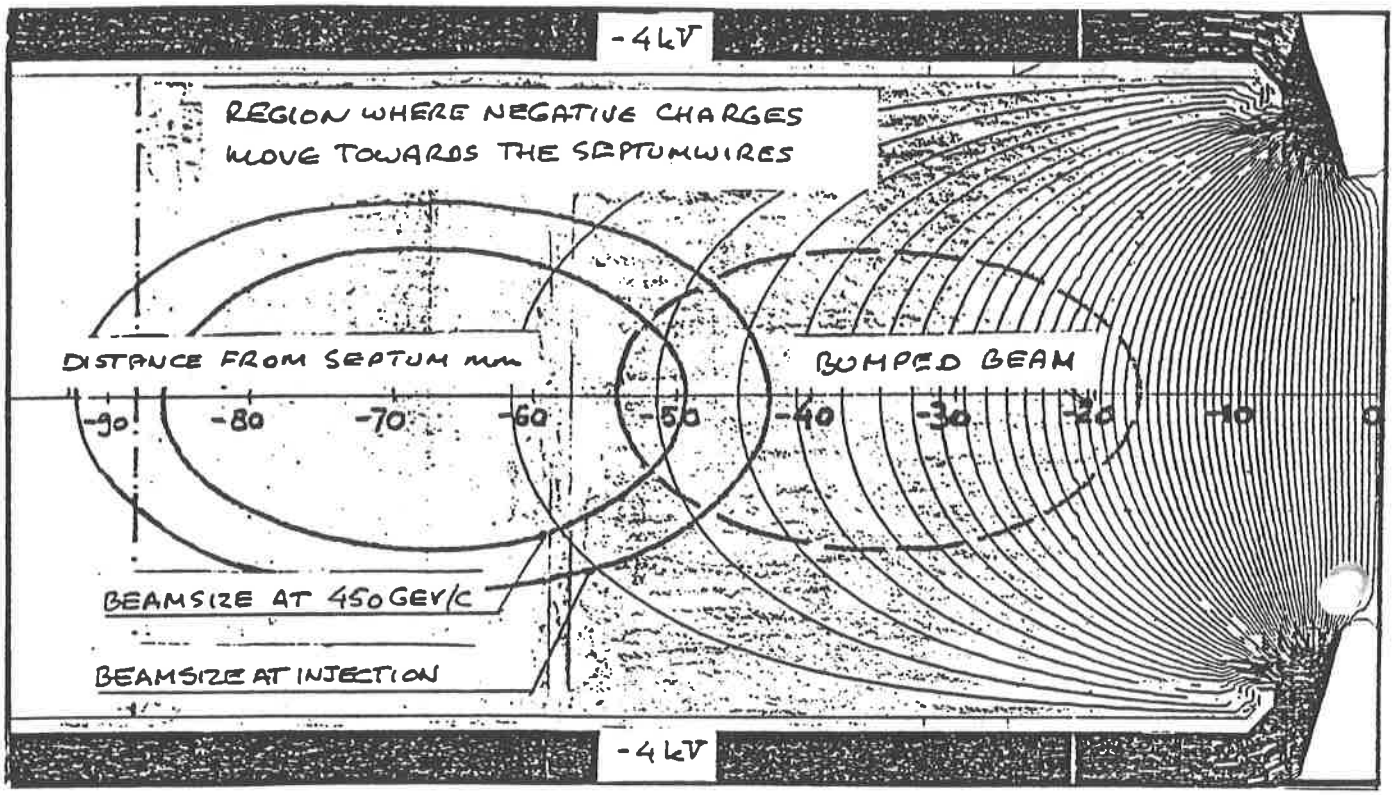

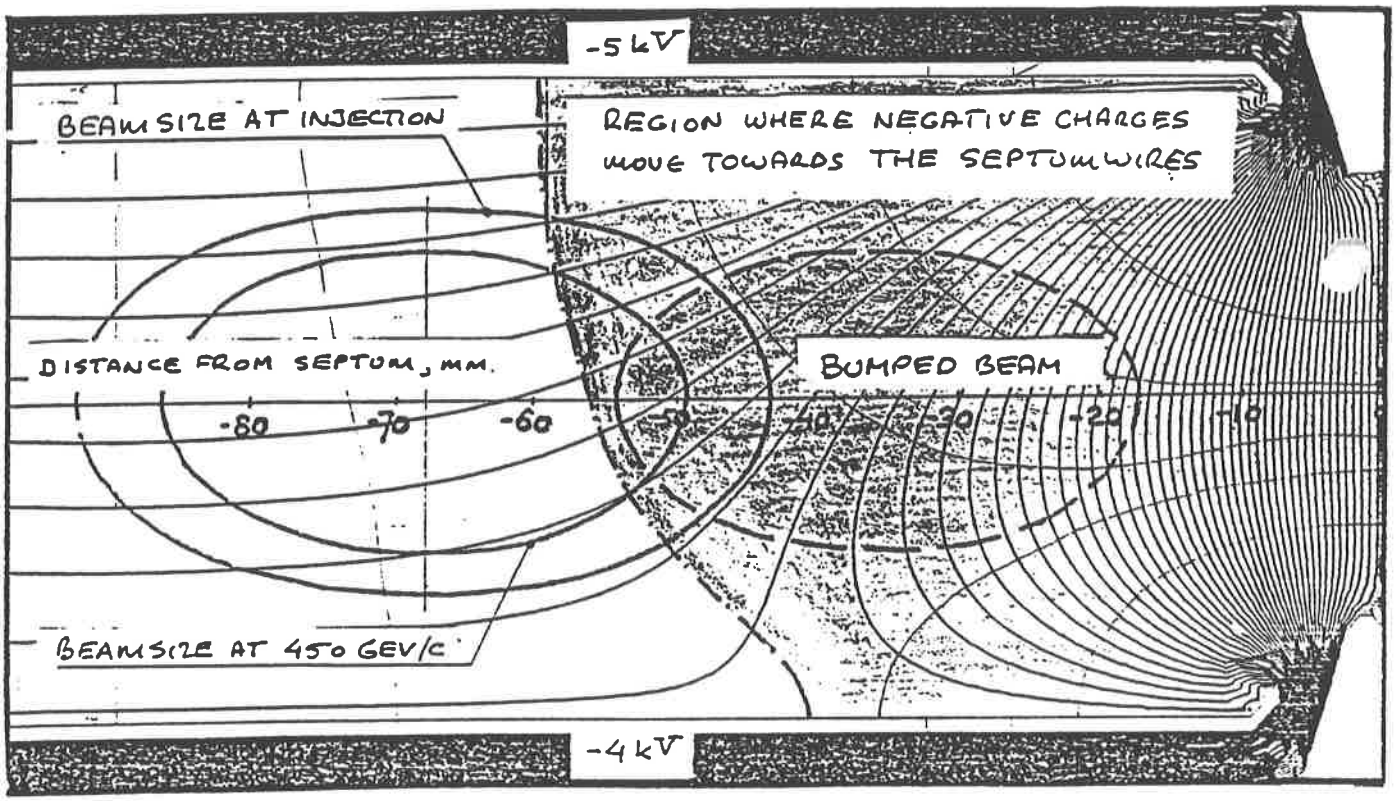

Fig. 14 Symmetrically and asymmetrically charged ion-traps

$$n_+ = \frac{k_2 P_+}{T_A} \qquad (25)$$

where P_+ is the N_2 equivalent ionisation pressure, in Torr and T_A the absolute temperature of the residual gas, K.

For the SPS[16] with a pressure P_+ of 10^{-7} Torr, $\sigma_N = 1.2\ 10^{-22}$ m^2, $l_{ei} = 3.3$ m, $k_2 = 9.65 \times 10^{24}$ m^{-1} K Torr^{-1} and $T_A = 300$°K the expected clearing current will be some 90 nA.

In reality the situation is much more complicated because of sputtering and gas desorption during extraction. Clearing currents of the order of 300 nA per 10^{13} p extracted have been measured under particular conditions when a leak in the vacuum system caused the pressure to rise to some 10^{-7} Torr.

4.2.3 Electrostatic fields

The POISSON programme has been used to improve the electrostatic fields inside the 15 kV feedthroughs and around the alumina stand-off insulators of the ion-traps.

The construction of the existing 15 kV feedthrough is shown in Fig. 1. The corresponding electric field is shown in Fig. 15, upper figure.

There are several imperfections:

- The presence of a threaded bolt, M4, used as a central conductor which generates fields of the order of 2×10^7 V m^{-1}, at 15 kV, at the tips of the thread.

- The electrical insulation consists of several ceramic rings allowing the field-emitted electrons to fall directly on the metal of the anode.

- High gradients of 6×10^6 V m^{-1} in the triple points, i.e. where the ceramic touches the negative anode in vacuum.

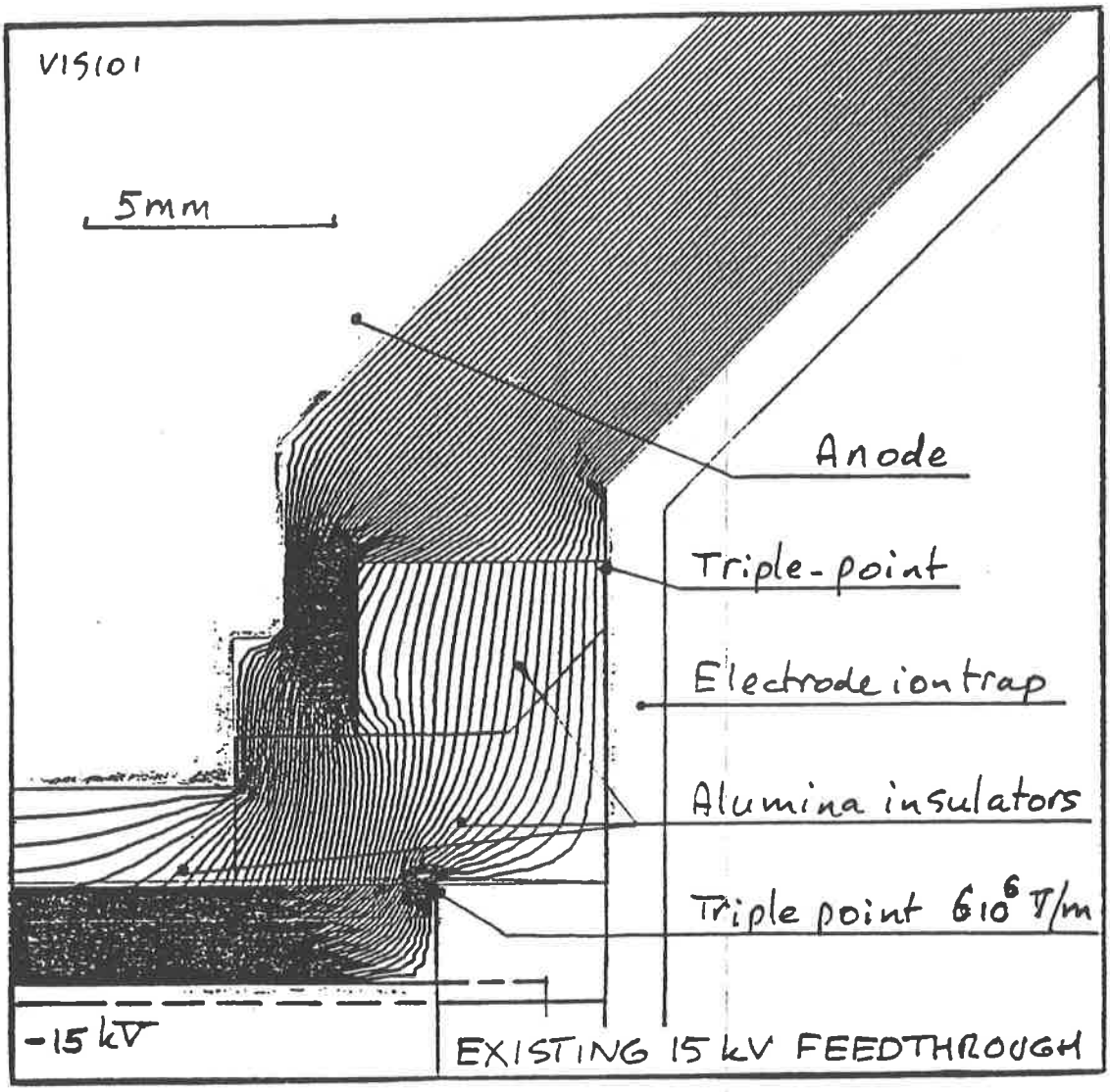

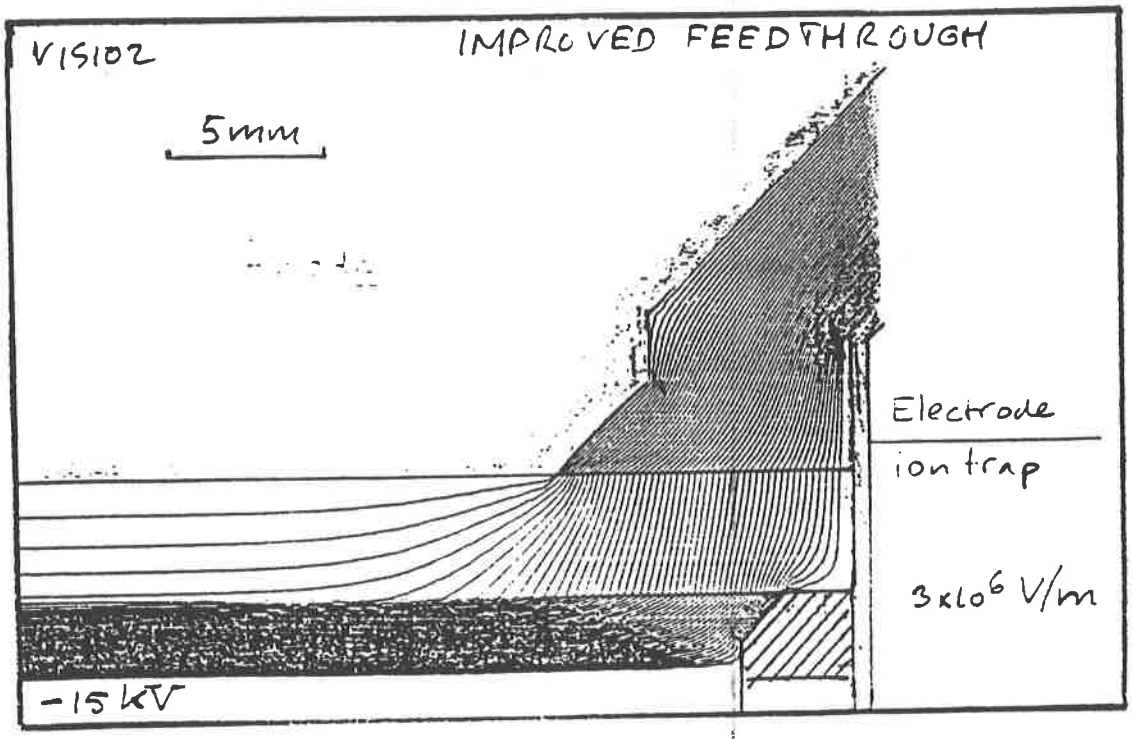

Fig. 15 The existing and the new feedthroughs

The construction of the improved feedthroughs is shown in Fig. 6 and the related field plots in Fig. 15, lower figure.

The improvements are as follows:

- The conductor is smooth and the diameter is adapted to the cylindrical insulation to create a minimum field strength.

- The dielectric medium consists of one cylinder only which is easy to machine and to mount and has many advantages from insulation point of view.

- In the triple point the gradient is reduced by some 50% and the field in the ceramic is much more homogeneous.

The construction of the existing stand-off insulators is shown in Fig. 1. Again complicated ceramic rings are used and the threaded bolt is negatively charged giving rise to field emission.

The field map, Fig. 16, shows that in the triple point fields of 3×10^6 V/m are created.

The construction of the improved insulators is shown in Fig. 6, upper figure, and the corresponding field maps in Fig. 17. By giving an appropriate angle to the ceramic, the fields are reduced in the triple points by a factor of 3.

7. Acknowledgements

The authors are indebted to S. Long who participated in the design of the improved electrostatic septa, and to R. Ducrêt who, together with Y. Sillanoni, assembled the new septa and solved many technical problems. Last but not least, the authors would like to thank K.H. Kissler who participated actively in many stages of the design, execution and organisation.

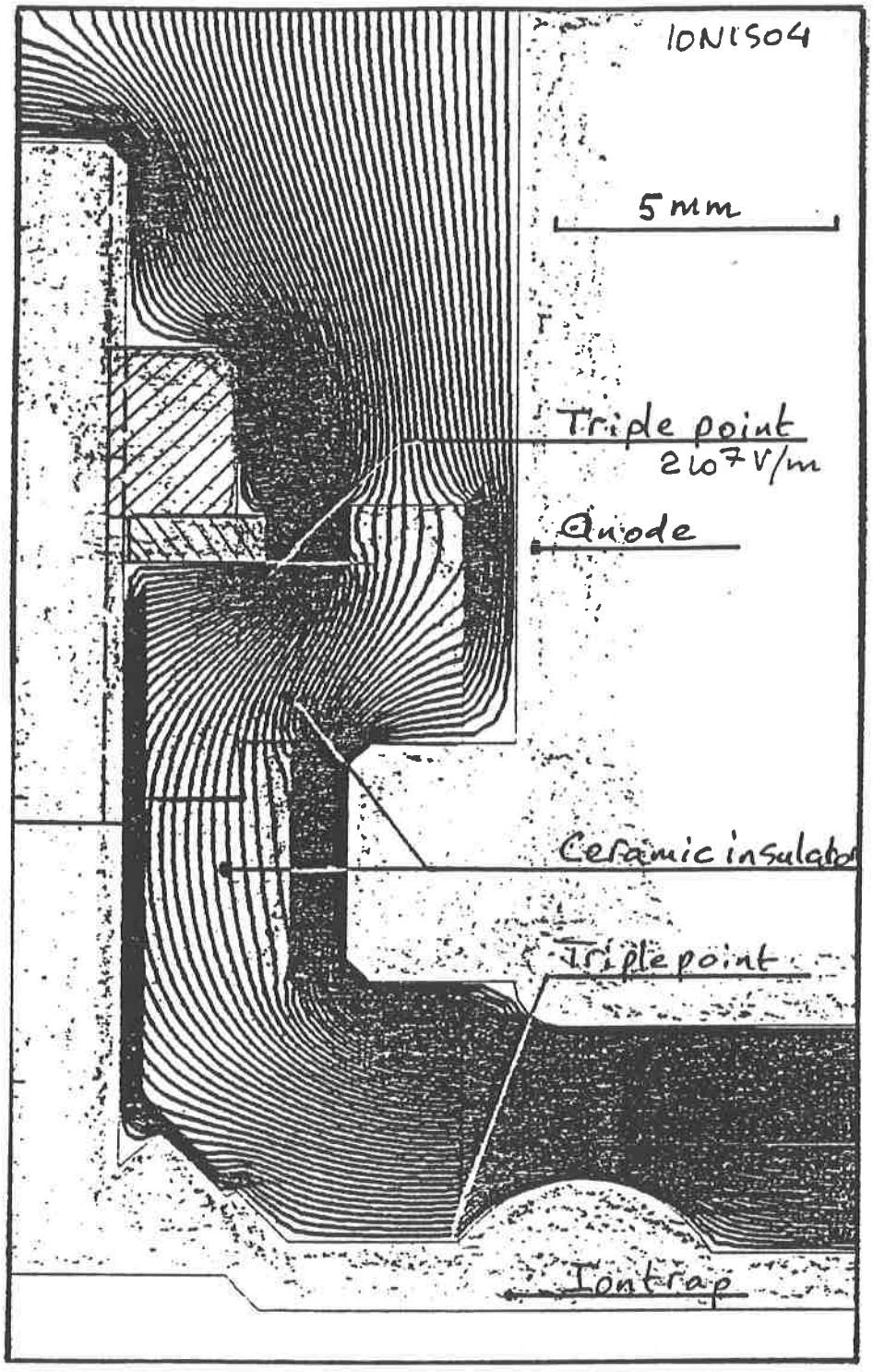

Fig. 16 Gradients and triple points in existing ion-traps

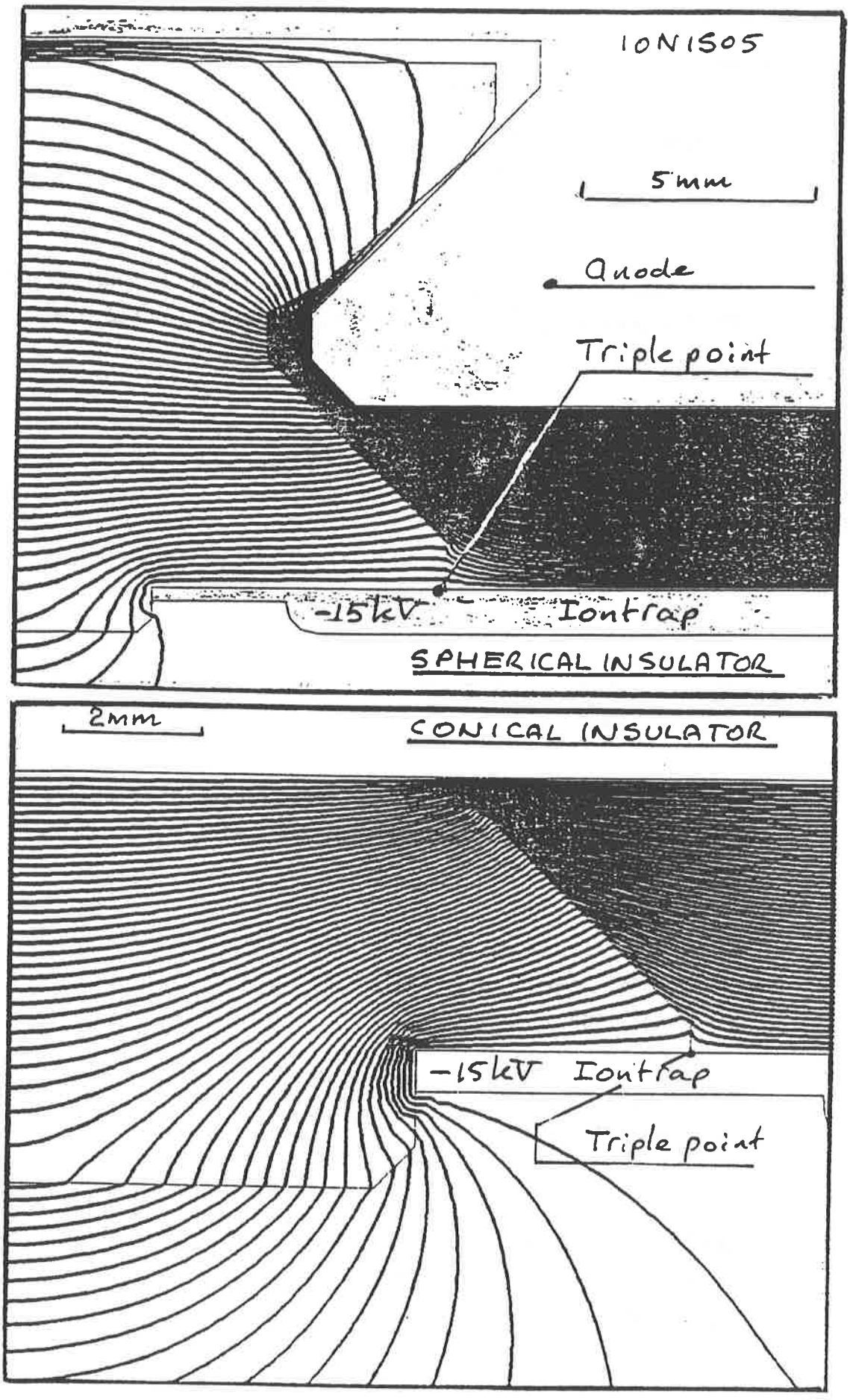

Fig. 17 New insulators for the ion-traps

8. References

1. Performance test of the electrostatic septum on 19.11.79. SPS Improvement Report No. 168 K.H. Kissler, dated 10th December, 1979.

2. Performance tests of the electrostatic septa during period 6C. SPS Improvement Report No. 171, K.H. Kissler, dated 3rd January 1980.

3. Essais du septum électrostatic en LSS6 avec extraction resonante rapide à haute intensité, SPS Improvement Report No. 178, K.H. Kissler, dated 12th March 1980.

4. SPS Improvement Report 185, K.H. Kissler, dated 24th July, 1980.

5. Spark rate analysis of the SPS electrostatic septa in LSS2 during period 7C, SPS/ABT/EX/RLK/Tech. Note 81-9, R.L. Keizer dated 15th December, 1981.

6. Observation of an increase of the effective thickness of the electrostatic septa SPS/ABT/Tech. Note/82-4, R.L. Keizer, 18th June, 1982.

7. Electrostatic septum tests in LSS6 with improved ion-traps, SPS Improvement Report No. 196, k.H. Kissler et al., dated 22nd November, 1982.

8. A solution to the increasing electrostatic septum thickness problem. SPS/ABT/Tech. Note/82-6, R.L. Keizer, 24th November, 1982.

9. Ionisation damage to the ZS electrostatic septa during periods 3, 4 and 5, 1983, SPS/ABT/Tech. Note/84-2, R.L. Keizer, 15th March, 1984.

10. Improved 300 kV feedthroughs for the SPS electrostatic septum SPS/ABT/Tech. Note 85-4, R.L. Keizer, et al., 2nd May 1985.

11. Analysis of ZS spark data immediately before and after the 1983/1984 shutdown, SPS/ABT/Tech. Note/84-3, R.L. Keizer, April 1984.

12. Improved extraction efficiency in LSS6 using INVAR Anodes and Ultra-thin septum wires, SPS/ABT/84-8. R.L. Keizer et al., 7th August, 1984.

13. Champ de fuite des septums électrostatiques à fils, A. Durand, P. Tanguy, D. Thouroude, Nucl. Instr. and Meth. 165, (1979) 361-370.

14. Roland Dubois, CERN/ABT, Private Communication.

15. Selection of formulae concerning proton storage rings. G. Guignard, CERN 77-10, dated 6th June, 1977.

16. The stability of ions in bunched beam machines, Y. Baconnier, G. Brianti, CERN/SPS/80-2 (DI).

17. H. Pastor, Rev. Int. Hautes Tempér. et Réfract., 1972 t.g, no.1 page 52-66.

18. Tension positive sur le septum électrostatique. R. Dubois, N. Garrel, SPS/ABT/NG/RD/Note Tech./78-4, 7th August, 1978.

APPENDIX 1 : HEAT TREATMENT OF THE INVAR BLOCKS

Prior and during machining the INVAR blocks have undergone the following heat treatment:

- During the fabrication of the blocks, annealed at 1050 °C, quenched in water.

- After rough machining, stabilisation at 400 °C during 6-8 hours suspended vertically.

- Machining of the pieces, oversize 1.5 mm stabilisation at 315 °C during 3 hours, suspended vertically.

- After electron beam welding stabilisation at 300 °C. Heating during 48 hours, flat top of 5 hours and cooling to 75 °C in 24 hours.

- Accelerated ageing at 100 °C during 24 hours, slow cooling at 25 °C/hour.

APPENDIX 2 : STRAIGHTNESS OF THE SEPTA

The septum has to be straight only in the median plane because the extracted beam is only a few mm high.

The horizontal deformations, d_1 and d_2, of the septum noses as shown in Fig. 18, are caused by two mechanisms:

- A vertical sag with amplitude s in the median plane combined with a rotation α about an axis somewhere in the median plane. Both parameters are zero near the ends, from where the septa are suspended. Because of the flexibility of the open profile, the contributions to the magnitude of d_1 and d_2 are different.

As has been mentioned in Section 3.1, the vertical plane is rendered straight within 10-20 μm by grinding the noses of the upper and lower blocks. The measured deformation is shown in Fig. 19, upper graph. The upper and lower noses have different deformations d_1 and d_2. The average deformation remains within 16 μm.

- An individual movement of the upper and lower blocks due to a pinching effect caused by the tensile forces in the 2000 septum wires. Although the amplitude of the individual displacements d_1 and d_2 is strongly increased, as in Fig. 19, lower figure shows, the average straightness is improved and is reduced from 16 to 12 μm.

On the 5 INVAR septa, the following straightnesses have been measured.

Anode No.	21	21	22	23	24
Straightness (μm)	12	14	10	16	11

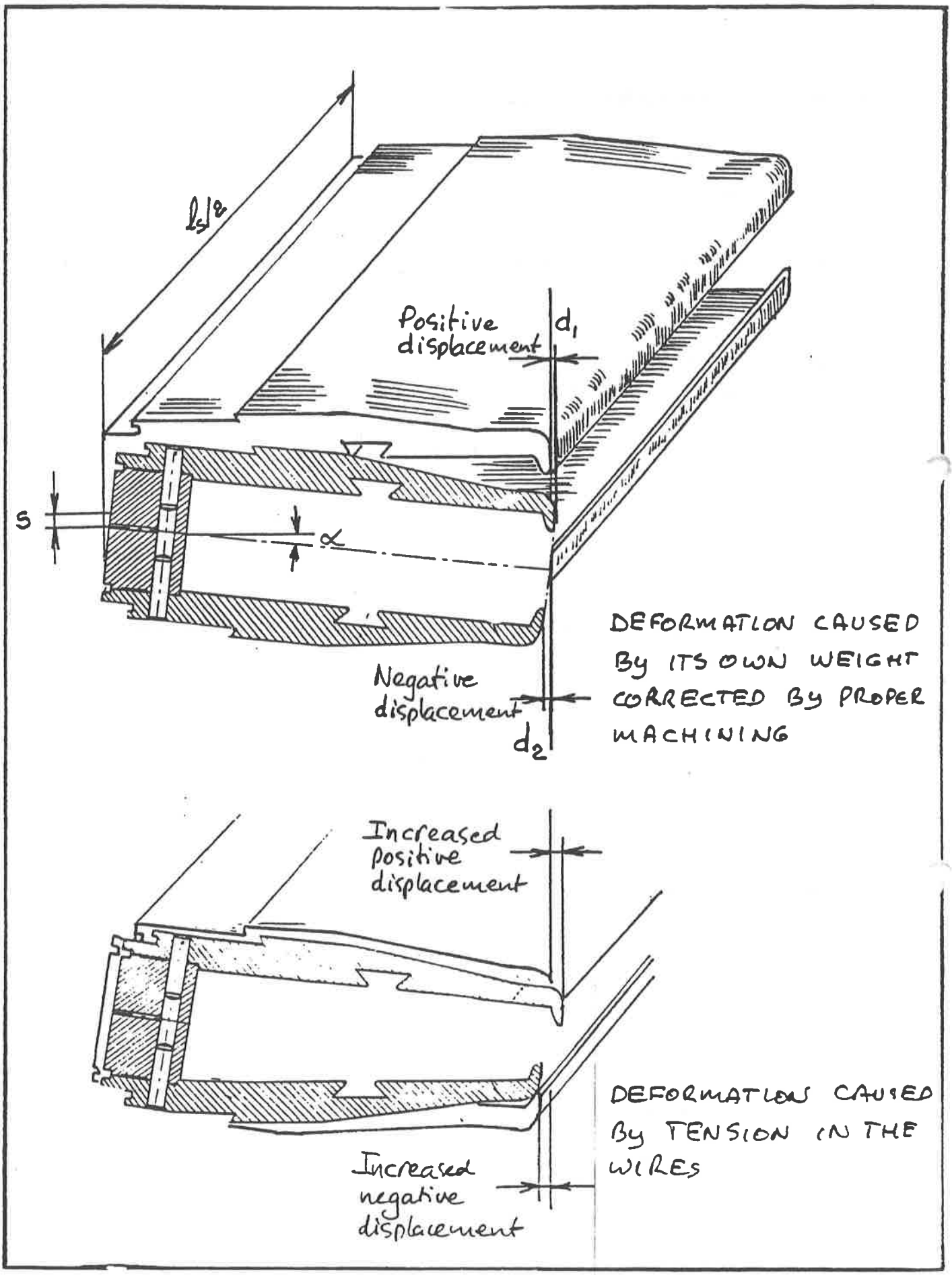

Fig. 18 Characteristic deformations of the anode

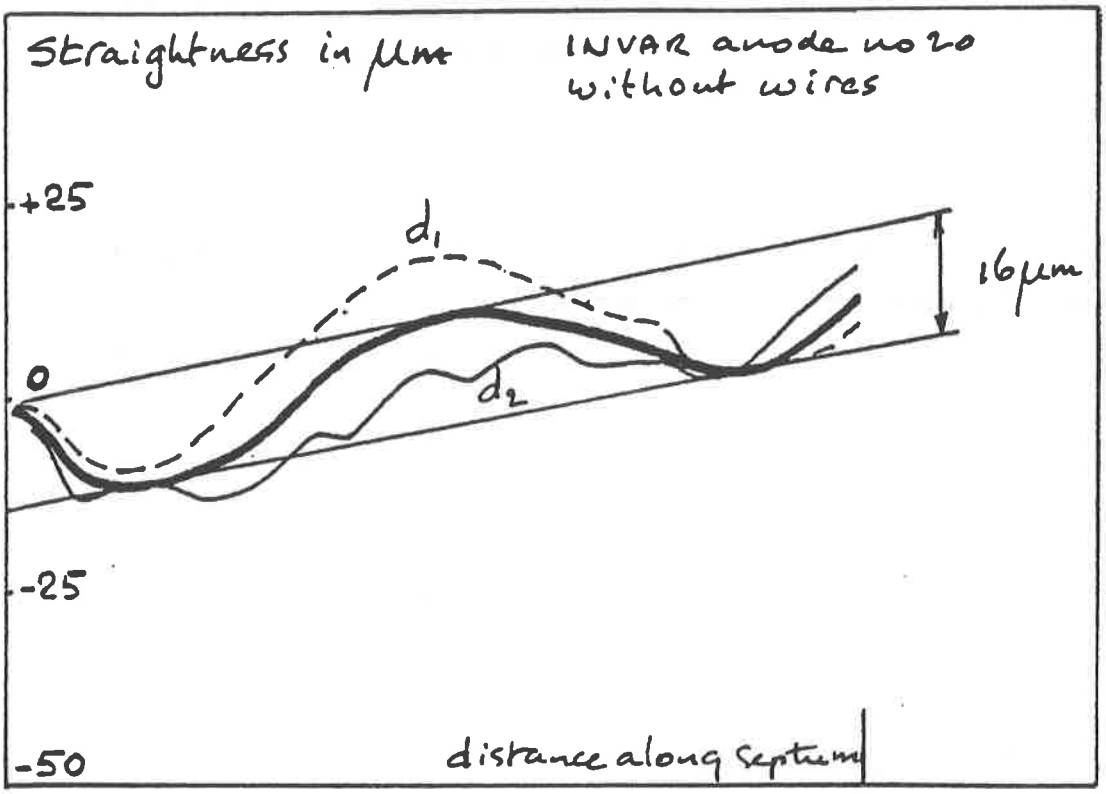

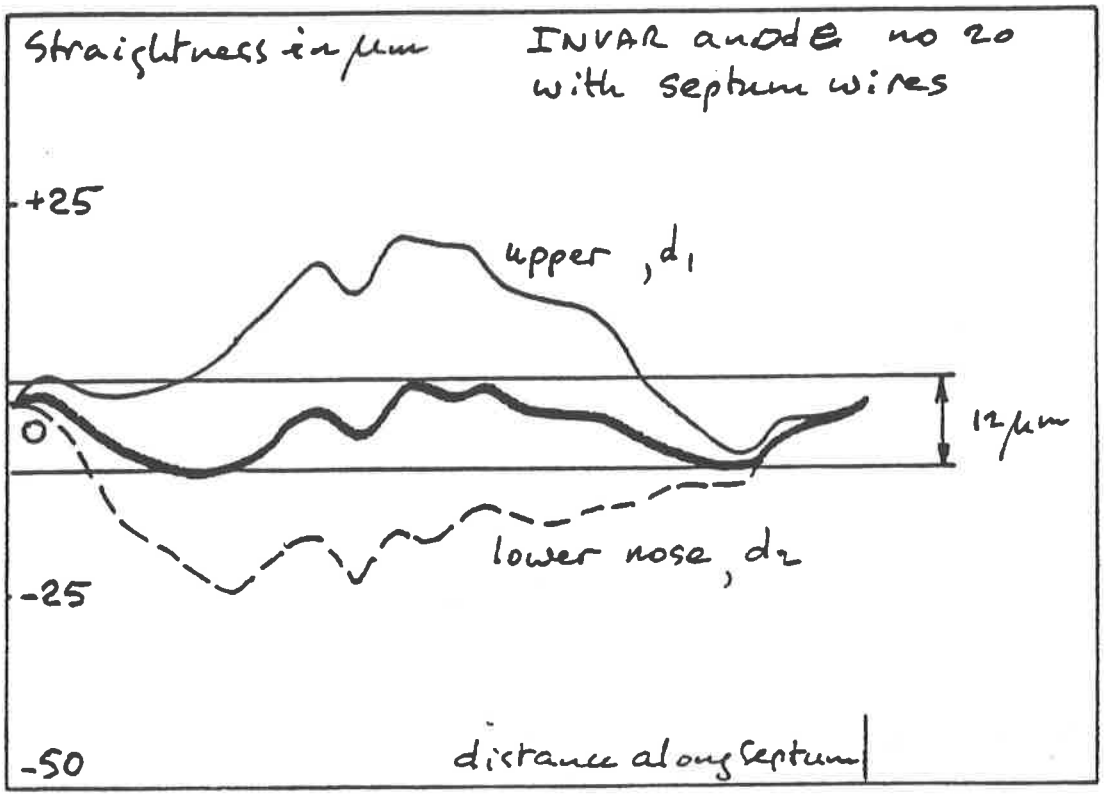

Fig. 19 Deformation of anode No. 20

APPENDIX 3 : DILUTION OF THE BEAM BY THE E.S. FIELD INSIDE THE SEPTUM PLANE

The average value of the transversal field component is calculated. Equation (17), Fig. 12 gives the expression for the transversal field $E_y(x,y)$. Calculate now the derivative

$$\left.\frac{\partial E_y}{\partial y}\right|_{\substack{y = 0 \\ x = \text{constant}}} = - \frac{\lambda \pi}{2 a^2 \varepsilon_o \left(1 - \cos \frac{2\pi x}{a}\right)} \tag{3.1}$$

The average value of the field gradient between $x = \frac{d}{2}$ and $x = \frac{a}{2}$ is then defined as:

$$G_y = \left\langle \frac{\partial E_y}{\partial y} \right\rangle \Bigg|_{\substack{y = 0 \\ \frac{d}{2} \leq x < \frac{d}{2}}} = \frac{V_g \ f_d}{h \ (a - d)} \left[\tan \frac{\pi \ d}{2 \ a} \right]^{-1} \tag{3.2}$$

A field gradient G_y over a width d is equivalent to a field E_y, where

$$E_{yo} = G_y \ d \tag{3.3}$$

causing a beam of width d to increase to width w_d at the downstream end of the septum.

The width of the electrostatically diluted beam is then defined as

$$w_d = d + \frac{10^{-3} \ E_{yo} \ l_e^2}{2 \quad \beta \quad p} \tag{3.4}$$

The percentage of protons removed from the septum plane assuming Gy to be constant over the entire width, is then given by

$$P_{pd} = 1 - \frac{d}{w_d}$$

With the values quoted in section 4.1.3 the average field $E_{yo} = 6.6 \times 10^{6}$ V m^{-1}. The beam width increases from d = 100 μm to w_d = 172 μm resulting in a proton loss from the septum plane of 42%.

APPENDIX 4 : NUCLEAR SCATTERING OF THE P BEAM IMPINGING ON THE SEPTUM

The assumption is made that the wires are rectangular in cross section. The transversal dimension is d. Longitudinally, the thickness is taken as the average thickness <d> where

$$\langle d \rangle = \frac{\pi}{4} d \tag{4.1}$$

If the drift space between the wires does not influence the scattering length λ_s then the proton flux after n wires is

$$N_n = N_o \exp \left(- \frac{10^{-6} \langle d \rangle n}{\lambda_s} \right) \tag{4.2}$$

The percentage of proton losses therefore is

$$P_{pn} = 100 \cdot \left[1 - \exp \left(- \frac{10^{-6} \pi d n}{4 \lambda_s} \right) \right] \tag{4.3}$$

For a WoRe septum with n = 2000 wires, d = 100 µm and λ_s = 0.1 m, the proton loss P_{pn} is 79%.

APPENDIX 5 : HEATING OF THE SEPTUM WIRES

The energy loss ΔE by ionisation of 450 GeV c^{-1} protons, minimum ionisation energy, is

$$\Delta E = 2.30\ 10^{-14}\ J\ kg^{-1}\ m^2 \tag{5.1}$$

The specific amount of heat ΔQ generated by N_o protons traversing some material with density is ρ_{wo} is

$$\Delta Q = N_o\ \Delta E\ \rho_{wo} \tag{5.2}$$

The average geometrical thickness <d> of a cylindrical wire with diameter d is

$$<d> = \frac{\pi}{y}\ d \tag{5.3}$$

The energy loss per wire is then ΔQ_w where

$$\Delta Q_w = <d>\ \Delta Q$$

$$= \frac{\pi}{4}\ d\ N_o\ \Delta E\ \rho_{wo} \tag{5.4}$$

The adiabatic temperature rise is then calculated as follows:

Assume that the horizontal proton distribution is homogeneous but is Gaussian vertically. The vertical distribution function f(z) is then given by

$$f(z) = f(o)\ \exp\ \left(-\ \frac{z^2}{2\ \sigma^2} \right) \tag{5.5}$$

$$f(o) = \frac{10^6\ N_o}{(2\pi)^{\frac{1}{2}}\ \sigma\ d} \tag{5.6}$$

when σ is the standard deviation. The beam height h_b is given by

$$h_b = 4\,\sigma . \tag{5.7}$$

The adiabatic temperature rise at the centre of the wire then becomes

$$\Delta T = \frac{4\ 10^{6}\ N_o\ \Delta E\ \rho_{wo}}{(2\pi)^{\frac{1}{2}}\ h_b\ d\ C_{wo}} \tag{5.8}$$

where C_{wo} is the specific heat.

For a WoRe wire, h_b = 0.003 m, C_{wo} = 2.7 x 10^{6} J m^{-3} $°C^{-1}$, ρ_{wo} = 1.92 x 10^{4} kg m^{-3}, N_o = 10^{11} ppp if a 1% loss is assumed and d = 100 µm. Therefore from (5.8) it follows that ΔT = 87 °C.

Equation (5.8) is valid if the diffusivity D_{wo} is small The diffusivity is defined as

$$D_{wo} = \frac{k_{wo}}{C_{wo}}\ m^2\ s^{-1} \tag{5.9}$$

where k_{wo} is the thermal conductivity. For WoRe wire k_{wo} = 1.75 x 10^{2} cm^{-1} $°C^{-1}$ and D_{wo} = 6.5 x $10^{-5} m^2$ s^{-1}. The hot spot on the wire is about 1.5 mm high and the heating time is typically 1 ms. Calculations show that the approximate time constant for the conduction of the heat along the wire is approximately 0.5 s. Therefore for fast and fast-slow resonant extraction the conditions are virtually adiabatic.

For extraction of intensities of 3 x 10^{13} ppp the expected temperature rise of the septum wires near the upstream end is therefore some 260 °C.